Title

Oxygen toxicity causes cyclic damage by destabilizing specific Fe-S cluster-containing protein complexes.

Journal

Molecular Cell, 83(6)

Authors

Haribowo, Augustinus
Chen, Xuewen
Queliconi, Bruno
et al.

Publication Date

2023-03-16

DOI

10.1016/j.molcel.2023.02.013

Peer reviewed

HHS Public Access

Author manuscript

Mol Cell. Author manuscript; available in PMC 2024 March 16.

Published in final edited form as:

Mol Cell. 2023 March 16; 83(6): 942–960.e9. doi:10.1016/j.molcel.2023.02.013.

Oxygen Toxicity Causes Cyclic Damage by Destabilizing Specific Fe-S Cluster-Containing Protein Complexes

Alan H. Baik[*,1,2], **Augustinus G. Haribowo**[*,2,3], **Xuewen Chen**[*,2,3,4], **Bruno B. Queliconi**[2,3], **Alec M. Barrios**[2,3], **Ankur Garg**[2,3], **Mazharul Maishan**[5], **Alexandre R. Campos**[6], **Michael A. Matthay**[5,7], **Isha H. Jain**[2,3,8,#]

[1]Department of Medicine, Division of Cardiology, University of California, San Francisco, CA, 94143, USA

[2]Gladstone Institutes, San Francisco, CA, 94158, USA

[3]Department of Biochemistry and Biophysics, University of California, San Francisco, CA, 94158, USA

[4]Biomedical Sciences Graduate Program, University of California, San Francisco, CA 94158, USA

[5]Cardiovascular Research Institute, UCSF, San Francisco, CA, 94143, USA

[6]Sanford Burnham Prebys Medical Discovery Institute, La Jolla, CA, 92037, USA

[7]Departments of Medicine and Anesthesia, University of California, San Francisco, CA, 94143, USA

[8]Lead Contact

SUMMARY:

Oxygen is toxic across all three domains of life. Yet, the underlying molecular mechanisms remain largely unknown. Here, we systematically investigate the major cellular pathways affected by excess molecular oxygen. We find that hyperoxia destabilizes a specific subset of Fe-S cluster (ISC)-containing proteins, resulting in impaired diphthamide synthesis, purine metabolism, nucleotide excision repair, and electron transport chain (ETC) function. Our findings translate to primary human lung cells and a mouse model of pulmonary oxygen toxicity. We demonstrate that the ETC is the most vulnerable to damage, resulting in decreased mitochondrial oxygen consumption. This leads to further tissue hyperoxia and cyclic damage of the additional ISC-

[#]Correspondence to Isha H. Jain, PhD. Isha.Jain@gladstone.ucsf.edu.
[*]equal contribution

AUTHOR CONTRIBUTIONS

IHJ, AHB, AGH, XC conceived the project, designed/analyzed experiments and wrote the manuscript. AHB, AGH, XC, BBQ, AMB, AG, MM, ARC, IHJ performed the experiments. IHJ and MAM supervised experiments. All authors reviewed the final manuscript.

DECLARATION OF INTERESTS

IHJ is a consultant for Maze Therapeutics and has patents related to hypoxia therapy for metabolic disorders.

INCLUSION AND DIVERSITY

We support inclusive, diverse, and equitable conduct of research.

containing pathways. In support of this model, primary ETC dysfunction in the *Ndufs4* KO mouse model causes lung tissue hyperoxia and dramatically increases sensitivity to hyperoxia-mediated ISC damage. This work has important implications for hyperoxia pathologies, including bronchopulmonary dysplasia, ischemia-reperfusion injury, aging, and mitochondrial disorders.

Graphical Abstract

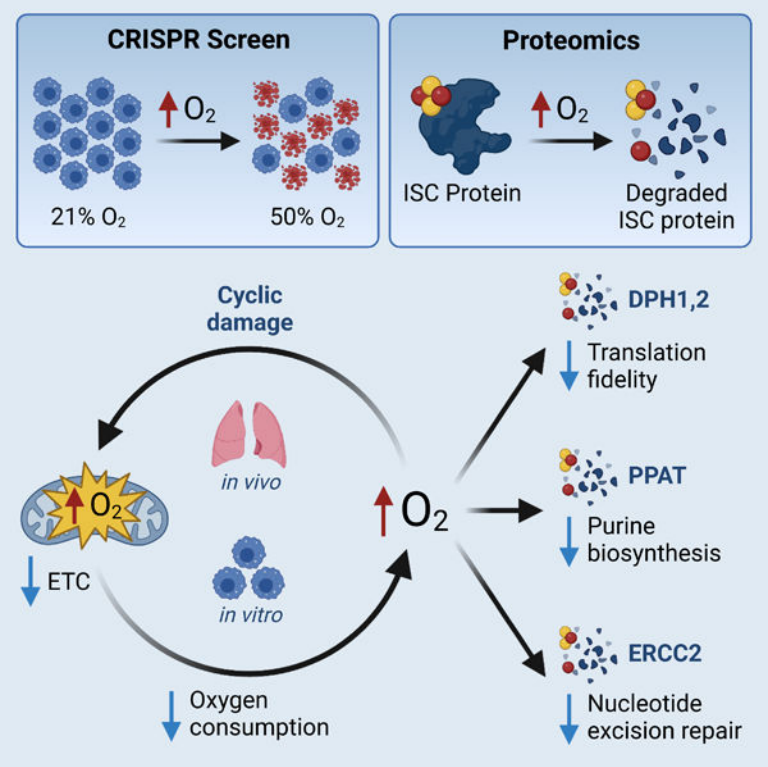

eTOC Blurb:

Baik et al. systematically investigate the major cellular pathways affected by excess molecular oxygen *in vitro* and *in vivo*. They find that hyperoxia impairs diphthamide synthesis, *de novo* purine biosynthesis, nucleotide excision repair, and ETC bioenergetics due to degradation of specific labile iron-sulfur cluster-containing proteins. Additionally, they prove a new model of cyclic oxygen toxicity.

INTRODUCTION

Approximately 2.5 billion years ago, the appearance of photosynthetic cyanobacteria led to the introduction of oxygen into Earth's atmosphere. This caused a mass extinction of species that lacked mechanisms required for survival in an aerobic environment[1,2]. Over the last 500 million years, atmospheric oxygen concentrations have fluctuated between 8% and 35%, with a current value of 21% O_2 at sea level. In response to such variations, organisms developed unique adaptive strategies. To avoid oxygen toxicity, some bacteria retreated to anaerobic environments such as deep-sea hydrothermal vents or the hypoxic

intestinal niche of symbiotic hosts[3,4]. Other organisms developed elaborate antioxidant defenses such as the glutathione redox system and superoxide dismutases[5,6]. During the Cambrian era when atmospheric O_2 peaked at ~35% O_2, insects became unusually large to limit oxygen diffusion to internal organs[7,8]. In higher organisms, the cardiovascular system evolved to precisely control oxygen delivery using vascular networks and hemoglobin as an oxygen-buffering system.

Thus, variations in oxygen tensions have driven responses to both oxygen deprivation (hypoxia) and excess (hyperoxia). Adaptation to hypoxia has been well-studied over the last few decades. For example, the hypoxia inducible factor (HIF) system marshals the primary transcriptional response to hypoxic environments[9–12]. In contrast, responses to hyperoxia have been less explored, even though hyperoxia is toxic across all species studied[13,14]. In the 1970s, the earliest work on oxygen toxicity showed that *E. coli* grew poorly in hyperbaric hyperoxia and became auxotrophic for branched chain amino acids, demonstrating that specific cellular pathways might be affected by oxygen[15–17]. These early findings inspired our current work on comprehensively understanding the cellular mechanisms of oxygen toxicity.

Higher organisms are also susceptible to oxygen toxicity, as demonstrated by classic observations in animals and humans from the late 19th century[18,19]. In modern medicine, millions of patients are treated with supplemental oxygen for acute and chronic illnesses[20,21]. In premature infants, this can result in bronchopulmonary dysplasia, which can lead to chronic lung disease and cor pulmonale[22,23]. Additionally, neonatal hyperoxia treatment can cause retinopathy of prematurity and blindness[24,25]. In the adult critical care setting, oxygen is one of the most frequently used therapies– for example, high flow nasal cannula can deliver oxygen up to 100% F_iO_2 at 60 L/min[26,27] (Supplemental Fig. S1A). However, emerging clinical data suggest that high-dose supplemental oxygen increases infarct size after myocardial infarction and impairs cardiac function[28,29], prolongs ICU admissions, and may increase mortality in mechanically ventilated patients[30–32].

Outside the setting of supplemental oxygen, tissue hyperoxia is implicated in a range of additional pathologies. For example, ischemia-reperfusion injury and obstructive sleep apnea are characterized by sudden bursts of oxygen[33,34]. Additionally, we recently showed that impaired electron transport chain (ETC) activity leads to brain hyperoxia in a mouse model of mitochondrial neurodegenerative disease[35]. The normalization of this hyperoxia by inhaled hypoxia increases lifespan by five-fold[36]. Therefore, understanding the mechanisms of oxygen toxicity will provide insights into numerous pathologies associated with tissue hyperoxia. Motivated by such diverse biomedical implications, we set out to understand a fundamental question to human health and biology – why is oxygen toxic?

Historically, researchers have focused on macroscale phenomena during hyperoxia and the broad concept of “oxidative stress” such as increased superoxide levels[37]. However, alleviating superoxide levels genetically or pharmacologically is insufficient to completely rescue oxygen toxicity[38–42]. Therefore, further investigation is warranted to understand downstream consequences of oxygen toxicity, as well as superoxide-independent mechanisms.

Here, we investigate the precise effects of hyperoxia on cellular metabolism and physiology. Using unbiased approaches, we demonstrate that four specific protein complexes are particularly sensitive to degradation in hyperoxia both *in vitro* and *in vivo* – DPH1/2, ERCC2, PPAT and the mitochondrial ETC. Notably, each of these structures contain a [4Fe-4S] cluster. While there are over 60 Fe-S(ISC)-containing proteins, these complexes are the most oxygen-labile. The downstream functional consequences include translational infidelity, impaired *de novo* purine synthesis, defective nucleotide excision repair and disrupted mitochondrial bioenergetics. Additionally, we propose a precise sequence of events that unfold in hyperoxia. The electron transport chain (ETC) is the "weakest link" and the first to be degraded as a function of time and oxygen. Hyperoxia-induced ETC degradation results in decreased tissue oxygen consumption, leading to even greater tissue hyperoxia. This cycle of toxicity continues, ultimately damaging the additional ISC-containing pathways.

RESULTS

Genome-wide CRISPR screen and proteomics reveal specific iron-sulfur cluster (ISC)-dependent cellular processes are inhibited in hyperoxia

Local oxygen tensions vary across and within organs. Therefore, we define "hyperoxia" as oxygen levels exceeding those to which a system has adapted. Since immortalized cells have been maintained in room air for generations, they display optimal survival at 21% O_2. We first determined the effect of hyperoxia on K562 cell fitness. We found that 50% O_2 dramatically impairs growth (Fig. 1A). Of note, 50% F_iO_2 in humans causes ultrastructural lung damage[43]. Additionally, this is a relevant O_2 level that is regularly achieved with non-invasive ventilation in patients (Supplemental Fig. S1A). Thus, we chose this physiologically- and clinically-relevant oxygen tension to detect the *most sensitive* pathways in hyperoxia. As we have previously noted, hypoxic conditions also result in impaired fitness at 1% O_2, suggesting a "Goldilocks principle of oxygen" where too little or too much oxygen is toxic[44,45]. Here, we set out to perform a genome-wide CRISPR knockout screen to identify pathways affecting hyperoxia cell fitness (Fig. 1B). We generated a genome-wide pool of K562 knockout (KO) cells using the Brunello CRISPR library[46]. Cells were then split into 21% (normoxia) or 50% O_2 (hyperoxia) (Fig. 1B). Samples were collected at 9 and 15 days post-treatment to track the depletion or enrichment of each KO. We observed a ~10,000-fold selection pressure in hyperoxia over the screen (Fig. 1C), allowing for identification of relative fitness in hyperoxia vs. normoxia.

We used the maximal likelihood estimate (MAGeCK-MLE) algorithm to compute gene essentiality in normoxia versus hyperoxia[47]. Genes were ranked based on their differential essentiality (Fig. 1D; Supplemental Fig S1B, C). "Buffering hits" include KOs that cause a growth defect in normoxia, but have epistatic interactions with hyperoxia. These pathways are likely defective in hyperoxia since KO of these genes does not further exacerbate the hyperoxia growth defect. On the opposite side, "sensitizing hits" are genes that are specifically required for survival in hyperoxia (Supplemental Fig. S1E).

To determine which pathways are affected by hyperoxia, we performed pathway enrichment analysis on the buffering genes. This highlighted several processes, including purine/IMP

biosynthesis, electron transport chain (ETC) complex assembly, diphthamide biosynthesis and folate metabolism (Fig. 1E). Initially, these pathways appeared unrelated. However, upon review of the literature, we learned that diphthamide synthesis could only be reconstituted *in vitro* under anaerobic conditions, due to the presence of an ISC that is susceptible to oxidation[48]. This led us to the key realization that the other affected pathways also rely on an essential step catalyzed by an ISC-containing protein. Moreover, genes involved in ISC assembly were more essential under hyperoxia than normoxia (Fig. 1D; Supplemental Fig. S1D, E).

Fe-S clusters (ISCs) are evolutionarily conserved cofactors that contain two or more iron ions bridged by sulfide ions. Approximately 60+ proteins are known to bind an ISC. These enzymes are required for diverse cellular functions, including redox reactions, amino acid synthesis and nucleotide metabolism[49]. ISCs are sensitive to oxidation, which can compromise their enzymatic activity. However, it is unknown which ISCs are sensitive to molecular oxygen, and if their damage is a major contributor to hyperoxic pathologies. Additionally, the downstream consequences and relevance *in vivo* are unexplored.

In protein purification protocols, ISC-containing proteins are unstable and precipitate under aerobic conditions[50,51]. We reasoned that if a similar phenomenon took place intracellularly under hyperoxia, it might lead to protein aggregation and degradation. To test this, we performed proteomics in K562 cells exposed to 21% or 50% O_2 for 6 days. Importantly, this revealed a significant overlap between depleted proteins and buffering hits in the CRISPR screen (Supplemental Fig. S1F). Of the 75 significantly depleted proteins, 14 were ISC-containing proteins (Fig. 1G) and most others were part of protein complexes that contained these subunits. Notably, we found that proteins with [4Fe-4S] clusters were most susceptible to hyperoxia-mediated depletion (Fig. 1G, H).

Upon analysis of the pathways containing the depleted proteins, we found that these proteins are involved in the mitochondrial ETC, diphthamide synthesis, DNA damage repair and purine synthesis (Fig. 1F, H). We observed a remarkable congruence between the most depleted proteins (based on proteomics) and most functionally affected pathways (based on CRISPR screen) in hyperoxia. We then performed an oxygen and time dose response analysis of the four most affected protein complexes. More specifically, we exposed K562 cells to 30–50% O_2 for 0–6d, followed by western blotting. We validated that hyperoxia leads to loss of these specific ISC-containing proteins (Fig. 1I–J). Notably, ETC subunits are by far the most sensitive to hyperoxia, showing depletion at moderate hyperoxia (30% O_2) at two days. This is particularly intriguing as patients are regularly treated with such moderate hyperoxia (Supplemental Fig. S1A).

Increased protein degradation is responsible for ISC protein loss in hyperoxia

To determine the mechanism by which these proteins are depleted in hyperoxia, we first investigated the corresponding transcript levels. The mRNA levels of these genes were unchanged in 50% O_2 (Fig. 2A). Next, we treated cells with cycloheximide to block translation. Hyperoxic cells still had higher depletion rates of the ISC-containing proteins, indicating damage downstream of translation (Fig. 2B). We then investigated mechanisms of protein degradation. We tested the role of proteasomal degradation and autophagy

using bortezomib and bafilomycin, respectively. Treatment with these inhibitors for 12h in hyperoxia partially rescued cytosolic PPAT, but not the other three protein complexes (Fig. 2C, D). Inducible knockdown of the proteasome subunit (*PSMA3*) also rescued PPAT (Supplemental Fig. S2A, C, E). We next investigated the mechanism of ETC subunit degradation which occurs by proteases rather than the proteasome[52]. We nominated 6 proteases localized to the matrix or inner membrane, of which only 2 are more essential in hyperoxia (YME1L1 and CLPP) (Fig. 1D, 2E, Supplemental Fig. S2B). We used CRISPRi to knockdown CLPP and YME1L1 (Supplemental Fig. S2C, D, F, G). CLPP KD partially rescued SDHB and NDUFS1 protein levels, suggesting that CLPP contributes to ETC protein degradation in hyperoxia (Fig. 2E). Together, our results demonstrate that proteasome- and autophagy-mediated degradation contribute to depletion of cytosolic PPAT and the mitochondrial protease CLPP contributes to ETC subunit degradation in hyperoxia.

Normalization of superoxide levels is insufficient to rescue hyperoxia-mediated loss of specific ISC-containing protein complexes

These results suggested that ISC oxidation leads to protein unfolding and degradation. The major ROS formed from molecular O_2 is superoxide $(O_2^{\bullet -})$ [53]. It has previously been noted that $(O_2^{\bullet -})$ can damage and inactivate ISC-containing proteins, such as aconitase. Thus, we sought to determine if the levels of the most oxygen-sensitive ISC-containing proteins could be rescued by normalizing superoxide levels. K562 cells were exposed to varying durations of 50% O_2. As expected, hyperoxia increased cytosolic and mitochondrial superoxide as detected by dihydroethidium (DHE) and MitoSOX, respectively (Fig. 2F, G). Cells were treated with saturating levels of the superoxide dismutase mimetic, MnTBAP, (Supplemental Fig. S2H, I) which dramatically reduced superoxide levels (Fig. 2F, G). Yet, ISC proteins from the four most sensitive pathways were not rescued (Fig. 2H). Saturating levels of H_2O_2 were also insufficient to deplete the labile ISC-containing proteins (Supplemental Fig. S2O). Together, our data show that superoxide is insufficient to explain protein depletion of the four most oxygen-sensitive ISC-containing proteins, suggesting that molecular oxygen itself might be the primary culprit.

Identical ISC-containing proteins are degraded in a mouse model of hyperoxic acute lung injury

We next assessed the physiological relevance of these pathways in a murine model of hyperoxia-induced lung injury. The lungs are at highest risk of oxygen toxicity due to their direct exposure to oxygen. In most mammals, including humans, exposure to 70% O_2 or higher leads to respiratory distress and acute lung injury[54–59]. Up to 100% supplemental O_2 with 60 L/min flow can be delivered to patients non-invasively with high-flow nasal cannula. The pathological features of hyperoxic lung injury resemble acute respiratory distress syndrome (ARDS), which is characterized by diffuse alveolar damage, inflammation, atelectasis, and microvascular coagulopathy, resulting in impaired gas exchange and hypoxemia[60]. While lung oxygen toxicity has been characterized at the macroscopic level, the effects of excess O_2 on ISC-containing proteins has not previously been studied in this setting.

To determine the effect of hyperoxia on the ISC-containing proteins described above and their downstream pathways *in vivo*, we exposed WT C57Bl/6 mice to 80% O_2. Consistent with prior studies, hyperoxia led to significant body weight loss (Fig 3B) and increased lung erythema and fluid retention. H&E staining revealed increased fibrinous exudate and hemoglobin infiltration (Fig. 3A; Supplemental Fig. S3A). There was a time-dependent increase in Evans blue dye extravasation in the lungs, reflecting increased vascular permeability of endothelial cells (Fig. 3A, 3D). We observed a significant increase in the lung wet-to-dry (W:D) ratio, reflecting increased pulmonary edema (Fig. 3C). We then asked whether the ISC proteins damaged in hyperoxic K562 cells were also affected in hyperoxic lung tissue. Remarkably, we observed a complete validation of these findings *in vivo* – the ISC-containing proteins (DPH1, ERCC2/XPD, ETC subunits and PPAT) in all four pathways were depleted in hyperoxic lung tissue (Fig. 3E, F). The ETC subunits in complex I and II were particularly sensitive to hyperoxia and were degraded within 24h of hyperoxia exposure, thus implicating the ETC as the weakest link in hyperoxia toxicity (Fig. 3H).

To interrogate the effects of hyperoxia on different cell types in mouse lungs, we used immunofluorescence to assess loss of one of the most oxygen-labile ETC proteins, NDUFS1 (complex I subunit) in relation to specific lung cell types in mice exposed to 21% O_2 or 80% O_2 for 5 days. We found that NDUFS1 protein levels were significantly depleted in alveolar epithelial type 1 (ATI) cells, type 2 (ATII) cells, and endothelial cells, demonstrating that each of these cell types is sensitive to oxygen toxicity (Fig. 3G; Supplemental Fig. S3D).

Identical ISC-containing proteins are degraded in primary human lung endothelial and epithelial cells under hyperoxia

Next, we assessed the susceptibility of these specific ISC proteins in various human lung cell types. We found that all four protein complexes were susceptible to hyperoxia in the BEAS-2B human lung epithelial cell line and A549 human alveolar basal epithelial cell line (Supplemental Fig. S3B, C). We then validated our findings in primary cells from human lung donors -- ATII cells (Fig. 3H) and endothelial cells (Fig. 3I). ISC proteins from all four pathways were decreased in hyperoxia. Our findings support the known susceptibility of pulmonary endothelial and alveolar epithelial cells to hyperoxia[37,61]. We now identify the molecular pathways that contribute to these macroscale changes under hyperoxic conditions in primary human cells and *in vivo* hyperoxic lung injury models. We focused our next investigations on the four most hyperoxia-sensitive pathways: (1) diphthamide synthesis, (2) purine metabolism, (3) nucleotide excision repair, and (4) mitochondrial bioenergetics.

Hyperoxia depletes DPH1 and DPH2 and impairs diphthamide synthesis

Diphthamide is a unique and understudied post-translational modification of a histidine residue on eukaryotic elongation factor (eEF2). Defects in DPH genes result in neonatal lethality[62]. While the exact function of diphthamide is unknown, it has been proposed to be required for translational fidelity[63]. Diphthamide is synthesized in a multi-step process, requiring 7 obligate enzymes DPH1–7[64]. Our genetic screen identified KOs in nearly all these genes as buffering hits (Fig. 4A). In matched proteomics, DPH1 and DPH2 were significantly depleted in hyperoxia (Fig. 4B). We confirmed that DPH1 and DPH2 protein levels are highly sensitive to excess O_2, demonstrating their declining levels as a function

of time and increasing O_2 tensions (Fig. 1I, 3E, H, I). The DPH1/DPH2 subunits form a heterodimer which contains a [4Fe-4S] cluster as a cofactor[48,65] (Fig. 4C). Notably, the other non-ISC-containing enzymes in diphthamide biosynthesis were not depleted in hyperoxia, despite being hits in the genetic screen. This result is consistent with the notion that knocking out one gene in the pathway disrupts the entire pathway, resulting in the observed genetic epistasis.

We next sought to determine the downstream effects of hyperoxia-mediated perturbations on diphthamide synthesis. Diphthamide is the target of the bacterial diphtheria toxin (DT), an enzyme that ADP-ribosylates diphthamide on eEF2, thereby causing steric hinderance for the ribosome and leading to cell death[66]. WT cells in normoxia showed a dose-dependent sensitivity to DT, whereas DPH1 and DPH2 KO cells were resistant to its toxicity. Similarly, hyperoxia conferred resistance to DT-mediated cell death in WT cells, demonstrating that the diphthamide modification is absent in hyperoxia due to loss of DPH1 and DPH2 (Fig. 4D).

To more directly test whether hyperoxia affects diphthamide synthesis, we visualized the modification with a custom assay relying on biotinylated-NAD as the substrate for ADP-ribosylation by DT[67]. In cells that contain eEF2-diphthamide, DT results in biotinylation of diphthamide, which can be monitored with HRP-streptavidin and western blotting. We observed a weakened band in cells with DPH1 or DPH2 KO (relative to WT cells in normoxia), as well as WT cells treated with hyperoxia (Fig. 4E). This assay confirmed that diphthamide synthesis is impaired in hyperoxia due to depletion of the DPH1/DPH2 ISC-containing protein complex.

We next investigated the functional consequences of DPH loss on protein translation. Diphthamide is thought to promote translational fidelity by preventing −1 ribosomal frameshifts[68]. To test whether hyperoxia-mediated loss of diphthamide compromises translation fidelity, we created a −1 frameshift luciferase reporter. This reporter contains a fusion protein of firefly luciferase and renilla luciferase with an intervening “slippery” sequence that causes increased rates of −1 frameshifting[69]. The firefly:renilla luciferase ratio indicates the extent of frameshifting, whereby higher values correspond to greater frameshift (Fig. 4F). We transfected the reporters into K562 cells exposed to 50% or 21% O_2 for 6 days and DPH1 or DPH2 KO cells in normoxia. Hyperoxic WT cells and DPH KO cells showed increased −1 frameshifting, which is consistent with the proposed role of diphthamide (Fig. 4F).

To test the *in vivo* physiological relevance of our findings, we investigated diphthamide loss in hyperoxic mouse lung tissue with the ADP-ribo-diphthamide western blot. We found that lung homogenate from mice exposed to 80% O_2 for 5 days had reduced DT-induced biotinylation of diphthamide (Fig. 4G), demonstrating that hyperoxia-mediated decrease of DPH1/2 impairs diphthamide synthesis *in vivo*. In summary, hyperoxia depletes the ISC-containing DPH1/DPH2, impairing diphthamide synthesis *in vitro* and *in vivo,* thereby resulting in translational infidelity.

Hyperoxia depletes PPAT and impairs *de novo* purine synthesis

Our pathway analysis highlighted genes involved in folate metabolism and purine biosynthesis as being affected by hyperoxia based on the CRISPR screen (Fig. 5A; Supplemental Fig. S4A). A likely link between folate and purine biosynthesis is that purine synthesis is the primary sink for 1C intermediates in proliferating cells[70]. Proteomics revealed only one significantly depleted protein in these pathways: phosphoribosyl pyrophosphate amidotransferase (PPAT), the rate-limiting enzyme in *de novo* purine biosynthesis (Fig. 5B,C Supplemental Fig. S4B). Consistent with our overarching hypothesis, PPAT is the only ISC-containing enzyme in these pathways (Fig. 5C). We confirmed the depletion of PPAT as a function of O_2 dose and duration (Fig. 1I, 3E, H, I). Based on these findings, we reasoned that genes in 1C metabolism and purine synthesis are buffering hits in hyperoxia due to destabilization of PPAT.

Next, we assessed the effects of hyperoxia on 1C metabolism. Dihydrofolate reductase (DHFR) is the first enzyme in this pathway, catalyzing the conversion of dihydrofolate to tetrahydrofolate. We used methotrexate (DHFR inhibitor) to phenocopy the loss of 1C metabolism. We found that methotrexate perturbed relative cell growth in 21% O_2 WT cells, but not PPAT KO cells. Similarly, WT cells exposed to 50% O_2 were also resistant, suggesting that 1C metabolism flux is decreased in hyperoxia (Fig. 5D; Supplemental Fig. S4C). These observations suggest that loss of PPAT under hyperoxia impairs *de novo* purine biosynthesis and decreases reliance on 1C metabolism.

To more generally assess this effect, we performed metabolomics in PPAT KO and WT K562 cells in normoxia and hyperoxia[71]. We observed significant overlap between changing metabolites in normoxic PPAT KO cells and hyperoxic WT cells (Fig. 5E, Supplemental Fig. S4D). As expected, the overlapping hits were enriched for purine metabolism intermediates (Supplemental Fig. S4E), including accumulation of PRPP, the upstream metabolite of PPAT enzyme activity (Fig. 5F). The levels of purine nucleotides (IMP, AMP, GMP) themselves were not affected. Of note, purines can be synthesized either through the *de novo* synthesis pathway or the salvage pathway. Thus, we predicted that the purine salvage pathway compensates for loss of PPAT in proliferating K562 cells. Consistent with this, levels of the salvage pathway precursors, xanthosine and xanthine, were decreased in both hyperoxic WT and normoxic PPAT KO cells (Fig. 5F).

We next assessed the *in vivo* physiological relevance of our findings. We performed metabolomics in lung tissue from WT mice exposed to 80% O_2 for 5 days and normoxic controls. We observed a substantial depletion of the purine nucleotides, AMP and GMP. Furthermore, the salvage pathway intermediates xanthine and xanthosine were also dramatically depleted (Fig. 5G, H). Indeed, purine-related metabolites were by far the most depleted metabolites using this unbiased approach. In contrast to proliferating cells, the salvage pathway is unable to completely compensate for PPAT loss in non-dividing lung tissue. These results demonstrate that hyperoxia compromises *de novo* purine synthesis *in vitro* and *in vivo* due to loss of the ISC-containing protein PPAT.

Hyperoxia depletes *ERCC2*/XPD, resulting in increased DNA damage and impaired nucleotide excision repair

We next turned our attention to the nucleotide excision repair (NER) pathway, since *ERCC2* was a top hit in the CRISPR screen and proteomics (Fig. 6A and B). *ERCC2* encodes the protein XPD, which is a [4Fe-4S]-containing protein that has helicase activity and is required for NER (Fig. 6C)[72–75]. We verified the time- and O_2 dose-sensitivity of *ERCC2*/XPD in hyperoxia (Fig. 1I, 3E, H, I). Though prior work has shown that excess O_2 increases DNA damage, it has been assumed to be related to non-specific oxidative stress[76–78]. We utilized the comet assay (single-cell gel electrophoresis) to detect DNA damage at the single-cell level. In this assay, increased DNA damage results in less supercoiling and the appearance of a "comet tail" upon gel electrophoresis. This assay demonstrated increased damage in WT cells exposed to UV light and normoxic ERCC2 KO cells. Similarly, comet tails were observed in WT cells exposed to hyperoxia (Fig. 6D).

The comet assay measures steady-state levels of DNA damage. In theory, this could be a consequence of increased production of DNA damage or decreased DNA damage repair. To distinguish between these possibilities, we performed a transfection-based assay to specifically quantify the rate of NER. We used UV light to introduce DNA damage (thymine dimers) into a luciferase-encoding plasmid (Fig. 6E; Supplemental Fig. S5)[79]. The damaged plasmid was then transfected into cells, and luciferase activity was measured as a readout of NER. Based on this assay, normoxic ERCC2 KO cells have impaired repair activity (Fig. 6E). We similarly observed this impairment in hyperoxia-treated WT cells.

Next, we tested the *in vivo* relevance of this finding. We isolated single cells from lung tissue from mice exposed to 80% O_2 for 5 days and normoxic controls. Cells from hyperoxia-treated mice had significantly increased DNA damage based on the comet assay (Fig. 6F). While DNA damage has previously been linked to oxidative injury, it has been assumed that this is due to increased rates of DNA damage production. Here, we demonstrate that impaired DNA damage repair due to loss of ISC-containing *ERCC2*/XPD is a significant contributor to this phenotype *in vitro* and *in vivo*.

Hyperoxia depletes ETC subunits and impairs ETC function

We next focused on the effects of hyperoxia on the electron transport chain (ETC). The mitochondrial ETC is composed of 5 protein complexes (C1-C5) and enables efficient ATP production, among other key metabolic roles. More than half of the ETC-encoding genes were buffering hits in hyperoxia (Fig. 7A). Additionally, we found that hyperoxia depletes 43 of 60 detected ETC proteins (Fig. 7B). Fe-S clusters are found in Complex 1, 2 and 3. Additionally, a single Fe-Cu structure is found in Complex 4. Notably, the mitochondrial ETC exists in structures known as supercomplexes, consisting of multiple ETC complexes (Fig. 7C). Therefore, hyperoxia-mediated damage to ISC-containing proteins leads to widespread depletion of ETC proteins, likely due to destabilization of mitochondrial complexes and supercomplexes. We validated the proteomics findings and found that protein levels of ETC subunits are rapidly decreased in hyperoxia, even after 2 days of moderate hyperoxia (30% O_2) (Fig. 1J, 3F, H, I).

We then tested the functional consequences of this finding using the mitochondrial seahorse assay in K562 cells exposed to 21% versus 50% O_2 from 0–6 days. We found a progressive decline in basal and maximal oxygen consumption rate (OCR pmol/min) as a function of time in 50% O_2, with >50% decline in OCR even after 2 days (Fig. 7D). These findings demonstrate that hyperoxia-induced degradation of ETC protein complexes impairs mitochondrial bioenergetics.

We then assessed the *in vivo* relevance in WT mice exposed to 80% O_2 for 1 and 5 days. We performed whole lung proteomics and found that specific substructures of C1 are the most depleted in hyperoxia. C1 consists of three modules – the NADH-oxidizing N-module, the CoQ containing Q-module and the proton-pumping P-module. A total of 8 ISCs are housed in the N and Q modules of C1 [80–82]. In line with this, these modules were the most depleted in our lung proteomics dataset in hyperoxia (Fig. 7E). Non-ISC containing subunits were also depleted in these models, suggesting secondary destabilization (Supplemental Fig. S6A, B). To understand the reversibility of the phenomenon, we analyzed the lung proteome of mice exposed to 80% O_2 for 5 days, followed by recovery of these mice in 21% O_2 for 1 and 5 days. Notably, the ETC subunit loss was reversible when mice were returned to normoxia (Fig. 7E, Supplemental Fig. 6A, B). To test the functional consequences of these findings, we isolated mitochondria from hyperoxic mouse lung tissue exposed to 21% O_2 versus 80% O_2 for 1–5 days. We observed a progressive loss in complex I/II-mediated oxygen consumption (Fig. 7F), consistent with progressive ETC dysfunction due to loss of ISC-containing proteins in these ETC complexes (Fig. 7E).

Hyperoxia-mediated ETC dysfunction results in further tissue hyperoxia and cyclic damage

Since hyperoxic lung samples displayed a severe loss of ETC subunits, we hypothesized that hyperoxia toxicity and mitochondrial ETC dysfunction might have overlapping pathologies. That is, whether the primary insult is hyperoxia or ETC inhibition, the downstream consequences might be similar. To assess this, we compared the results of our screen to previously published CRISPR screens using ETC inhibitors - piericidin A (complex I inhibitor), antimycin A (complex III inhibitor) and EtBr (mtDNA replication inhibitor)[83]. We also included a H_2O_2 CRISPR screen[84] (Fig. 7G). This analysis revealed significant overlap in the top buffering genes between hyperoxia and ETC inhibitors, (Supplemental Fig. S7A) supporting the notion that both insults have similar pathological mechanisms. Notably, there was minimal overlap between hyperoxia and the H_2O_2 screen (Fig. 7G). Additionally, most known antioxidant enzymes were not hits in our CRISPR screen or proteomics, further suggesting that hyperoxia toxicity and primary ROS-inducing insults are not completely synonymous (Supplemental Fig. S2M, N).

Of the ISC-containing protein pathways described, the ETC subunits (particularly the N and Q module of C1) were the most dramatically affected – both in terms of oxygen dose and duration. In theory, ETC dysfunction should lead to decreased oxygen consumption in tissues. We predicted that such a decrease in oxygen consumption should lead to further tissue hyperoxia, resulting in a form of cyclic damage. To test this, we measured lung tissue PO_2 (using a 100-micron Clark electrode) in mice that had been exposed to 80% O_2 for 0–5 days. Of note, the average alveolar size in mice is ~60 microns[85]. We found that mice

exposed to hyperoxia for several days typically had higher lung tissue PO_2 compared to controls (Fig. 7H).

Ndufs4 KO mice have increased sensitivity to hyperoxic ISC damage, causally demonstrating the model of cyclic oxygen toxicity

The above results supported our theory that the ETC (particularly C1 N and Q modules) is the first to be affected and the most sensitive to hyperoxia. We therefore nominated the ETC as the weakest link in oxygen toxicity (Fig. 7C, E). We hypothesized that hyperoxia first damages the N and Q modules of C1, which decreases mitochondrial oxygen consumption. This results in further tissue hyperoxia, causing damage to additional ISCs. To causally test this, we utilized a genetic mouse model of C1 N-module deficiency, the *Ndufs4* KO. Though WT mice survive in 50% O_2 for greater than 2 years, *Ndufs4* KO mice die within 72 hours due to severe pulmonary edema and inflammatory cell infiltration (Fig. 7I and J, Supplemental Fig. S7B)[86]. We found that *Ndufs4* KO mice experience severe endothelial dysfunction based on Evans blue dye extravasation compared to WT mice at 50% O_2 (Fig. 7I, K). Importantly, we also found that the same ISC proteins that were depleted in WT mice at 80% F_i O_2, were depleted even in 21% F_iO_2 in *Ndufs4* KO mice (Fig. 7M). We reasoned that ETC dysfunction in *Ndufs4* KO mice increases levels of unused O_2 in lung tissue, resulting in higher local PO_2 levels and ensuing oxygen toxicity in other cell compartments. To test this, we measured lung tissue PO_2 using a Clark electrode in WT and *Ndufs4* KO mice at P35–40 days. This revealed lung tissue hyperoxia in *Ndufs4* KO mice across varying levels of inhaled oxygen tensions (Fig. 7L). These data are consistent with a clinical study that showed that venous PO_2 is higher in patients with mitochondrial myopathy compared to healthy controls due to impaired O_2 consumption[87].

Together, these data support our model that hyperoxia causes ETC dysfunction due to degradation of ISC-containing subunits, leading to decreased tissue oxygen consumption and further local hyperoxia. This progressive hyperoxia eventually damages the additional ISC-containing protein complexes in various subcellular compartments, compromising diphthamide biosynthesis, purine biosynthesis, and nucleotide excision repair (Fig. 7N).

DISCUSSION

Oxygen is both essential and toxic for life. While responses to hypoxia have been extensively studied, the specific molecular effects of hyperoxia are less understood. Though prior oxygen toxicity research has focused on tissue-level phenomena such as inflammation and non-specific oxidative injury, the molecular mechanisms involved have not been determined[60,88]. Thus, we set out to answer a fundamental question in biology - why is oxygen toxic?

Utilizing a genome-wide CRISPR/Cas9 screen, we identified four cellular pathways that are the most susceptible to hyperoxia due to depletion of labile ISC-containing protein complexes:(1) diphthamide synthesis, (2) purine metabolism, (3) nucleotide excision repair, and (4) the electron transport chain. These findings validated *in vivo*, where cyclic damage to the ETC causes progressive tissue hyperoxia and increased sensitivity to oxygen.

In-solution, researchers have proposed that oxygen oxidizes [4Fe-4S] clusters, which could destabilize neighboring cysteines and compromise protein stability[89]. This likely explains why ISC-containing proteins precipitate when purified in aerobic conditions[48]. However, this concept has not been studied within eukaryotic cells or mammals. Our work demonstrates that oxidation of specific ISC-containing proteins results in protein destabilization both *in vitro* and *in vivo*. Though there are greater than 60 ISC-containing proteins, we find that only a specific subset is particularly susceptible to damage by oxygen. The specificity may be due to biophysical parameters (e.g., pK_a of neighboring cysteines, solvent accessibility, local redox environment, relative positioning of cysteines)[90]. It is possible that additional ISC-containing protein complexes are sensitive at higher O_2 concentrations or longer durations. In addition, previous work has suggested that hyperoxia may affect ISC assembly, alluding to an additive form of cyclic damage in extreme hyperoxia[91,92] (Fig. 7N).

Our work points to a fascinating evolutionary conundrum -- oxygen is both a substrate and a toxin for the ETC. The original insult can originate via tissue hyperoxia or primary mitochondrial disease. In both scenarios, the cycle of damage ensues, resulting in degradation of additional ISC-containing proteins. Future investigation will focus on testing the four most sensitive pathways in additional models of mitochondrial disease, aging, Parkinson's and ischemia-reperfusion injury[93]. If the same pathways are affected, future work will test the effects of inhaled hypoxia on halting cyclic oxidative damage. It will also be interesting to investigate the relevance of our findings to additional organs and disease states. Large-scale meta-analyses and randomized control trials demonstrate that excess supplemental oxygen worsens outcomes in patients with myocardial infarction, cardiac arrest, brain injury, and critical illness[94–97] – we hypothesize these effects are partly due to tissue hyperoxia. In addition, supplemental oxygen is administered to millions of patients both acutely and chronically (e.g., heart failure, COPD, COVID-19, etc.)[95,98,99]. Damage to the identified ISCs might be a significant contributor to such pathological states.

In addition to the oxygen-labile ISC proteins we identify, there are likely additional contributors to oxygen-mediated cellular toxicity. We find that superoxide is insufficient to explain the degradation of the four most oxygen-sensitive ISC-containing protein complexes. However, SOD1 and SOD2 are sensitizing hits in our CRISPR screen (Supplemental Fig. S2M), suggesting that superoxide likely contributes to hyperoxia toxicity through damage of additional biomolecules. Notably, molecular oxygen can diffuse across membranes, whereas superoxide typically acts where it is formed. Other antioxidant enzymes (e.g. catalase) and NRF2 targets are not hits in our screen and are unlikely to be principal drivers of ameliorating hyperoxia toxicity[100,101] (Supplemental Fig. 2K–N). Thus, our work suggests that antioxidant therapies are unlikely to be curative, further motivating our efforts to understand the downstream metabolic consequences of hyperoxia toxicity.

Several key unanswered questions remain. How are damaged ISC-containing proteins repaired? Our *in vivo* proteomics data show that ETC subunit depletion is reversible through unknown signaling cascades. We identified the mechanism of protein degradation for a subset of depleted proteins. More comprehensively, which protein quality control mechanisms mitigate hyperoxia damage? Based on the oxygen dose response experiments

and the hyperoxia sensitivity of *Ndufs4* KO mice, the ETC appears to be the most susceptible to hyperoxia toxicity. Can we target the "weakest link" for therapeutic benefit, thereby preventing the cyclic damage that follows? Prior work has shown that a single amino acid substitution in the ISC-containing fumarate nitrate reduction protein in *E. coli* increases cluster stability, protecting it under aerobic conditions[102]. Furthermore, our genetic screen identified > 200 sensitizing genes in hyperoxia – loss of these genes aggravates growth defects in hyperoxia, suggesting that these genes are essential for hyperoxic cell fitness.

Based on the above concepts, we propose that every individual has an optimal oxygen "set-point" based on genetic background, age, altitude, and underlying co-morbidities. Along these lines, we recently found that ETC C1 deficiency leads to brain hyperoxia, which is mitigated by inhaled hypoxia[35,36]. Others have discovered that the mouse model of Friederichs's ataxia has impaired ISC biogenesis, which can be partially rescued by inhaled hypoxia[103]. Based on our findings, we nominate additional disorders that might be susceptible to hyperoxia such as xeroderma pigmentosum (*ERCC2*/XPD loss)[104], diphthamide-deficiency syndrome (DPH1/2 loss)[105], and other ETC deficiencies. Moreover, genetic variants in any of 60+ ISC-containing protein complexes may increase susceptibility to oxidative protein destabilization.

For the past several decades, oxygen research has focused on hypoxia sensing and adaptations, such as PHD-HIF and mTORC1 signaling[44,106]. However, hyperoxia sensing mechanisms are poorly understood. Given our evolutionary origins in both hypoxic and hyperoxic environments, it is highly likely that there are conserved hyperoxia sensing pathways that allow cells to adapt to such conditions. Furthermore, little is known about physiologic adaptations to hyperoxia and consequences of chronic oxygen toxicity, which could be relevant for aging and chronic cardiopulmonary diseases that require long-term, high FiO_2 therapy.

LIMITATIONS OF THE STUDY

In this manuscript, we validate ISC protein susceptibility to oxygen toxicity in ATII and endothelial cells. Future studies should assess additional lung cell types. We performed the genome-wide CRISPR KO screen in the highly tractable K562 cell line, then performed targeted experiments in more relevant *in vitro* and *in vivo* experimental systems. Genome-wide CRISPR screens in primary lung cells are not currently technically feasible, though would complement the current study once tractable. Though we distinguish the effects of oxygen and superoxide, future work should investigate the mechanisms by which specific free radicals differentially affect individual ISCs.

STAR METHODS

RESOURCE AVAILABILITY

Lead Contact:

- Further information and requests for resources and reagents should be directed to and will be fulfilled by the lead contact, Isha H. Jain (Isha.Jain@gladstone.ucsf.edu)

Materials availability

- Plasmids generated in this study have been deposited to Addgene (pAGH10 – RlucFluc minus 1 HIV-1 (#198224); pAGH11-RlucFluc plus 1Ty1 (#198225)).

DATA AND CODE AVAILABILITY

- Raw sequencing data for the CRISPR screen have been deposited to SRA (PRJNA931848). Raw data for proteomics studies have been deposited to MassIVE database (MSV000091206). Raw data for metabolomics have been deposited to MetaboLights (MTBLS7039). They are publicly available as of the date of the publication. Unprocessed images of western blots, gels, and microscopy can be accessed from Mendeley Data: http://dx.doi.org/10.17632/ykcyz2sdx2.1.
- No original code was generated for this manuscript.
- Any additional information required to reanalyze the data reported in this paper is available from the lead contact upon request.

EXPERIMENTAL MODEL AND SUBJECT DETAILS

Cell lines—K562 (ATCC CCL-243), 293T (ATCC CRL-3216) and A549 (ATCC CCL-185) cells were purchased from ATCC. K562 cell line with doxycycline-inducible KRAB-dCas9 construct was a gift from Luke Gilbert Lab at UCSF, generated by Gilbert et al. [107]. K562 and 293T cells were maintained in DMEM (Gibco/Life Technologies 11995073) supplemented with 10% FBS (Corning/Fisher Scientific MT35015CV) and 1% penicillin-streptomycin-glutamine (Fisher Scientific 10378016). A549 cells were maintained in F-12K medium (ATCC 30–2004) supplemented with 10% FBS and 1% penicillin-streptomycin-glutamine. BEAS-2B (CCLZR505) cells were obtained from UCSF Cell Culture Core Facility, and were maintained in BEGM Bronchial Epithelial Cell Growth Medium with Bullet Kit (Lonza CC-3170). Human pulmonary artery endothelial cells (HPAEC, Promocell C-12241) were maintained in Endothelial Cell Growth Medium (PromoCell C22010). Human alveolar Type II epithelial (AT II) cells were isolated from human lungs declined for transplantation by the Northern California Transplant Donor Network as previously described [108]. Cells were plated at 1×10^6 cells/well on collagen I-coated Transwell plates with a pore size of 0.4 μm and a surface area of 0.33 cm^2 (Corning CLS3495, Sigma). Cells were maintained in DMEM high glucose 50%/F-12 50% mix supplemented with 1% penicillin-streptomycin, 1% fungisome and 0.1% gentamicin. At 72 hr after seeding, the culture media in the upper compartment was removed and the cells were grown in an air-liquid interface.

All cells were maintained in cell culture incubators (37°C, 5% CO_2). The oxygen tension in the hyperoxia cell culture incubator (50% O_2) was created by mixing compressed air and 100% O_2 (Praxair). All experiments with wildtype (WT) cells or CRISPR-Cas9 mediated knockouts were performed within 20 passages upon receipt. All experiments with primary lung cells were performed within 6 passages upon receipt. Cells were maintained at a density between 1 x 10^5 cell/ml to 1 x 10^6 cell/ml for all experiments. Mycoplasma tests were performed quarterly on all cell lines.

Animal model—C57BL/6J (#000664) male mice and B6.129S4-Ndufs4$^{tm1.1Rpa}$/J (#027058) were purchased from Jackson Laboratory. Upon delivery, the mice were housed in the UCSF animal facility. Progenies from the B6.129S4-Ndufs4$^{tm1.1Rpa}$/J strain were genotyped and weaned from mothers at 21–25 d of age. Ndufs4$^{+/+}$ and Ndufs4$^{+/-}$ mice were indiscriminately used as healthy controls as there was no apparent phenotypical difference between these genotypes.

Hyperoxia (60 or 80% O_2) was created by mixing N_2 (Airgas) and O_2 (Airgas, Praxair) inside a glovebox. The gas flow rates were carefully controlled by gas regulators, and the O_2 and CO_2 levels were continuously monitored with wireless sensors. Soda lime (Fisher Scientific, A1935236) was placed inside the glovebox to absorb CO_2 to prevent excess CO_2 accumulation. All experiments were performed on C57BL/6J mice between the ages of 8–12 weeks. All animal studies were approved by the Institutional Animal Care & Use Program (IACUC) at UCSF.

METHODS DETAILS

Genome-wide CRISPR KO screen—The genome-wide CRISPR screen was performed in K562 cells as previously described [45]. Briefly, 1.20 x 10^8 cells were diluted to 1.50 x 10^6 cells/mL and mixed with 4 mg/mL polybrene. Cells were plated in 12-well plates and infected with the Brunello Human CRISPR Knockout Pooled Library (Addgene, #73179-LV) at an MOI of 0.3 [46]. The plates were centrifuged at 1,000g for 2hr for 32°C for spinfection. Infected cells were selected with 2 μg/mL puromycin (Sigma-Aldrich, P8833) for 24hr, then pooled in magnetic spinner flasks (Corning, 3561). Five days after infection, 4.0 x 10^7 cells were passaged in complete media without puromycin (P0) into separate spinner flasks and placed into either 21% or 50% O_2 cell culture incubators. Cells were subsequently passaged every 3 days during the 15-day screen. Cells were collected, pelleted, and frozen at every passage (P0 to P5). The experiment was performed in biological duplicate. Samples from P0 (day 0), P3 (day 9) and P5 (day 15) were sequenced. Genomic DNA was extracted from cell pellets with the Blood and Cell Culture DNA Maxi Kit (Qiagen, 13323). The sgRNAs were amplified by PCR. PCR products were then pooled and purified with AMPure XP beads (Beckman Coulter, A63880). Equal amounts of each sample were pooled and sequenced at UCSF Center for Advanced Technology (CAT).

Proteomics—Sample processing and LC-MS/MS was performed by Sanford Burnham Prebys using the Tandem Mass Tag (TMT) system for the cell samples, and data-independent acquisition for lung tissues (see below).

Label-free proteomics for lung tissues—C57BL/6J mice (n = 6 per group) were exposed to room air or 80% O_2. For the recovery groups, the mice were exposed to 80% O_2 for 5 days first, and then transfer to room air. Tissues were perfused with cold DPBS. Lung tissues were collected and flash frozen with liquid nitrogen. Lung tissues were lysed in 8M urea, 50mM ammonium bicarbonate and 24U/100mL benzonase with vigorous shaking. Lysate was centrifuged at 14,000xg for 10 minutes to remove debris, and protein concentration of the supernatant was determined using bicinchoninic acid (BCA) protein assay (Thermo Scientific, 23225). Proteins were reduced with 5mM tris (2-carboxyethyl)

phosphine (TCEP) at 30°C for 60 min. Subsequently, protein lysates were alkylated with 15mM iodoacetamide (IAA) in the dark at room temperature for 30 min. Next, 50 mM ammonium bicarbonate was added to dilute urea to 1M, and protein lysates were mixed with ammonium bicarbonate and digested with mass spec-grade trypsin/Lys-C mix (1:25 enzyme/substrate ratio) overnight. The digested samples were loaded onto AssayMap reverse-phase resin small pore (C18) cartridges on an Agilent AssayMap Bravo platform. Samples were acidified with 0.1% formic acid and peptides were eluted with 60% ACN and 0.1% formic acid. Finally, the organic solvent was removed in a SpeedVac concentrator.

Prior to LC-MS/MS analysis, dried peptides were reconstituted with 2% ACN, 0.1% FA and concentration was determined using a NanoDropTM spectrophometer (ThermoFisher). Samples were then brought to the same concentration and spiked with iRT (Biognosys) analyzed by LC-MS/MS using a Proxeon EASY-nanoLC system (ThermoFisher) coupled to an Orbitrap Fusion Lumos mass spectrometer (Thermo Fisher Scientific). Peptides were separated using an analytical C18 Aurora column (75μm x 250 mm, 1.6 μm particles; IonOpticks) at a flow rate of 300 nL/min (60°C) using a 118-min gradient: 2% to 6% B in 1 min, 6% to 23% B in 72 min, and 23% to 34% B in 45 min (A= FA 0.1%; B=80% ACN: 0.1% FA). The mass spectrometer was operated in positive data-independent acquisition mode. MS1 spectra were measured in the Orbitrap in a mass-to-charge (m/z) of 350 – 1100 with a resolution of 120,000 at m/z 200. Automatic gain control target was set to 4 x 105 with a maximum injection time of 50 ms. Then the instrument was set to fragment (HCD) 56 x 10 m/z precursor isolation window DIA spectra with a 0.5 m/z window overlap, ranging from 400 to 900 m/z (15,000 resolution, normalized AGC target 500% and maximum inject time 20 ms). All samples were acquired using block randomization to avoid bias.

TMT proteomics for cell samples—K562 cells were plated in 10-cm dishes and maintained in 21% or 50% O_2 for 6 days. Equal number of cells were harvested and were flash frozen with liquid nitrogen. Three independent biological replicates were collected. Cell samples were lysed and processed with the same protocol above. Following drying, equal amounts of peptides were used for TMT labeling using a TMT-to-peptide ratio of 3:1. Peptides were reconstituted directly in 50% acetonitrile in 50mM HEPES (pH 8.5) containing one of the TMT tags from the TMT10plex reagent (Thermo Fisher). Labeled peptide samples were then pooled and dried using a SpeedVac system, and subsequently reconstituted in 0.1% FA for desalting using a C18 TopTip (PolyLC, Columbia, MD) according to the manufacturer's recommendation. The organic solvent was removed in a SpeedVac system. Dried pooled sample was reconstituted in 20 mM ammonium formate pH ~10 and fractionated using a Waters Acquity BEH C18 column (2.1x 15 cm, 1.7 μm pore size) mounted on an M-Class Ultra Performance Liquid Chromatography (UPLC) system (Waters). Peptides were then separated using a 35-min gradient: 5% to 18% B in 3 min, 18% to 36% B in 20 min, 36% to 46% B in 2 min, 46% to 60% B in 5 min, and 60% to 70% B in 5 min (A=20 mM ammonium formate, pH 10; B = 100% ACN). A total of 36 fractions were collected and pooled in a non-contiguous manner into 18 total fractions. Pooled fractions were dried to completeness in a SpeedVac concentrator prior to mass spectrometry analysis.

Dried peptide fractions were reconstituted with 2% ACN, 0.1% FA and analyzed by LC-MS/MS using a Proxeon EASY nanoLC system (Thermo Fisher Scientific) coupled to

an Orbitrap Fusion Lumos mass spectrometer (Thermo Fisher Scientific). Peptides were separated using an analytical C18 Aurora column (75μm x 250 mm, 1.6μm particles; IonOpticks) at a flow rate of 300 μl/min using a 75-min gradient: 1% to 6% B in 1 min, 6% to 23% B in 44 min, 23% to 34% B in 28 min, and 27% to 48% B in 2 min (A= FA 0.1%; B=80% ACN: 0.1% FA). The mass spectrometer was operated in positive data-dependent acquisition mode. MS1 spectra were measured in the Orbitrap with a resolution of 60,000 (AGC target: 4e5; maximum injection time: 50 ms; mass range: from 350 to 1500 m/z). The instrument was set to run in top speed mode with 3 s cycles for the survey and the MS/MS scans. After a survey scan, tandem MS was performed in the Ion Routing Multipole HCD-Cell on the most abundant precursors by isolating them in the quadrupole (Isolation window: 0.7 m/z; charge state: + 2–7; collision energy: 35%). Resulting fragments were detected in the Orbitrap at a resolution of 50,000 (First mass: 110 m/z; AGC target for MS/MS: 1e5; maximum injection time: 105 ms). The dynamic exclusion was set to 20 s with a 10 ppm mass tolerance around the precursor and its isotopes.

Generation of CRISPR KO and inducible CRISPRi cell lines—The plasmid containing lentiCRISPRv2 backbone (AddGene #52961) was digested and ligated with sgRNAs (Table S6) as previously described [109]. The CRISPRi backbone plasmid was a gift from Martin Kampmann Lab at UCSF. The backbone plasmid was digested and ligated with sgRNAs (Table S6). Lentiviruses were generated by co-transfecting HEK293T cells (ATCC CRL-3216) with the packaging plasmids pVSVg (AddGene 8454) and psPAX2 (AddGene 12260). Transduction was performed by spinfection as described previously [36] in WT K562 for CRISPR KO, and K562 expressing dCas-KRAB fusion protein for CRISPRi. Cells were selected in culture media containing puromycin (2 μg/mL) for 2 days.

For CRISPR KO, the Cas9-induced double-strand breaks are known to induce non-homologous end joining (NHEJ) which results in random indels; therefore, the knockout cells likely consist of a heterogeneous mixture of mutants, including hypomorphs. To avoid enriching for hypomorphic mutants, all experiments with pools of knockouts were performed within 18 days post spinfection.

Western blotting—For protein extraction, K562 cells and lung tissues were lysed with ice-cold RIPA buffer (ThermoFisher PI89901) supplemented with cOmplete Protease Inhibitor Cocktail (Roche). Lung tissues were homogenized using the Qiagen Tissue Lyser II (30 Hz, 1min) and steel beads (Qiagen) in RIPA buffer, followed by sonication. Equal amounts of protein (20–30μg) were mixed with 6X Laemmli SDS sample buffer (Fisher Scientific, AAJ61337AD). Samples were boiled at 95°C for 5min. Protein lysates were loaded on SDS-PAGE gels (Bio Rad Mini-PROTEAN® TGX™) and run at constant voltage. Proteins were transferred onto PVDF membranes using Trans-Blot Turbo (Bio Rad, 1704157) according to the manufacturer's instructions. Membranes were blocked with 2% non-fat milk (Genesee Scientific Corporation 20–241) in TBST (Fisher Scientific 28360) for 1hr at RT on a rocker. The membranes were probed for primary antibodies overnight at 4°C. The corresponding secondary antibodies were applied to the membranes in 5% non-fat milk for 1hr at RT. The antibodies and concentrations are listed in Table S6. Bands were visualized using ECL (Fisher Scientific PI32106) according to the manufacturer's

instructions. All experiments were conducted in biological triplicates. One representative western blot is shown for each experiment.

Antioxidant treatment and superoxide measurement—MnTBAP (Millipore Sigma, #475870) was dissolved in 75 mM NaOH. K562 cells were treated with various dosage of MnTBAP. The maximal tolerated concentration (500 μM) was chosen for superoxide measurement.

MitoSOX Red (Thermo Fisher M36008) was dissolved in DMSO, stock 2.5mM. Cells were exposed to 21 or 50% O_2 with or without 500uM MnTBAP for up to 3 days. Equal number of cells were resuspended in basal media with or without MnTBAP. MitoSOX was added to each solution for a final concentration of 5uM and incubated at 37°C for 20 minutes. DHE (Thermo Fisher D11347) was dissolved in DMSO, stock 5mM. Cells were exposed to 21 or 50% O_2 with or without 500uM MnTBAP for up to 3 days. Equal number of cells were pelleted for each condition. Cells were resuspended in basal media with or without MnTBAP. DHE was added to each solution for a final concentration of 10uM and incubated at 37°C for 60 minutes.

Rotenone was used a positive control for both experiments. Cells were washed with HBSS without phenol red (Thermo Fisher, #14025076) twice, transferred to flow cytometry tube through 35um cell strainer, and kept on ice in the dark. Both MitoSOX and DHE signals were measured via flow cytometery with 405nm excitation and 610+/−20nm emission using 600LP LongPass mirror. 10K events were measured in technical duplicate. All reagents were pre-equilibrated in 21% and 50% O_2 prior to use in the assay. The cells in 50% O_2 were cultured and handled in a glove box with gas control for all steps until transferred to flow cytometry tubes.

ADP-ribosylation assay—The assay was performed as previously described [66,67] with modifications. Diphtheria toxin (DT) (Millipore Sigma, D0564) was mixed 9:1 with 10 mg/ml trypsin (Sigma-Aldrich T7168, in H_2O) for 15 min, resulting in nicking of full-length DT (concentration 1μg/μl). The reaction was stopped with saturated cOmplete Protease Inhibitor Cocktail solution (Sigma-Aldrich 11697498001, 1 tablet/ml dissolved in H_2O).

K562 cells with DPH1 KO, DPH2 KO or Dummy sgRNA were maintained in 21% or 50% O_2 incubators for 6 days. Upon harvesting, cells were lysed with RIPA buffer (ThermoFisher PI89901) supplemented with cOmplete Protease Inhibitor Cocktail. Lung tissues harvested from mice exposed to room air or 80% O_2 for 5 days were homogenized using the Qiagen Tissue Lyser II (30 Hz, 1min) and steel beads (Qiagen) in RIPA buffer supplemented with cOmplete Protease Inhibitor Cocktail, followed by sonication. Following lysis, the protein extract from cells or tissues (200 μg) was mixed with 2μg nicked diphtheria toxin in ADP-ribosylation buffer (20 mM Tris-HCl, pH 7.4; 1 mM EDTA; 50 mM Dithiothreitol) with 10 μM 6-Biotin-17-NAD (Trevigen 4670–500-01, 250 μM) in a total volume of 120 μl. The mixture was incubated at 25°C for 30min. The reaction was stopped with 6X SDS sample buffer. Samples were boiled for 5min. Both *in vitro* and *in vivo* experiments were performed in biological triplicates.

Diphtheria toxin (DT) sensitivity assay—K562 cells with DPH1 KO, DPH2 KO or Dummy sgRNA were plated at 1 x 10^5 cell/ml in 10-cm dishes and maintained in 21% or 50% O_2 incubators for 6 days. The cells were passaged on day 3 to prevent confluency. Cells were treated with diphtheria toxin (Sigma D0564) for 3 days in their corresponding oxygen levels. Cell numbers were determined by CellTiter-Glo (Promega G7573) according to the manufacturer's instructions. Experiments were performed in 3 independent biological replicates.

Translational fidelity assay—Dummy cells (with 6-day pre-treatment under 21% or 50% O_2), DPH1 KO and DPH2 KO were plated into 12-well plates. The cells were transfected with the HIV-1 or Ty1 expression vectors shown in Figure 4F using Lipofectamine LTX (Life Technologies, 15338100) according to the manufacturer's instructions. The cells were incubated in their corresponding oxygen conditions for 48hr. The cells were harvested, washed with DPBS and resuspended in 160μl DPBS at room temperature. Equal volumes of cell suspension were plated into opaque 96-well assay plates in duplicate. The firefly and luciferase luminescence were measured using the Dual-Glo luciferase assay (Promega E2920) according to the manufacturer's instructions. The ratios of firefly to renilla luminescence were calculated to quantify ribosomal translational frameshifts. The experiment was conducted in 6 independent biological replicates.

Methotrexate treatment—Dummy and PPAT KO cells were generated from K562 cells with the sgRNA sequences listed in Table S6. Dummy cells were pretreated with 21% or 50% O_2 for 6 days. Cells were seeded on opaque clear-bottom 96-well plates at a starting density of 1 x 10^4 cell/ml. Methotrexate hydrate (Sigma-Aldrich, A6770) was dissolved in 1M NaOH and then diluted with DPBS. Cell were treated with methotrexate for 3 days under normoxia (21% O_2) or hyperoxia (50% O_2). Cell viability was determined by CellTiter-Glo (Promega G7573) according to the manufacturer's instructions. The experiment was performed in 3 independent biological replicates.

Metabolomics—Dummy cells were plated at 1 x10^5 cell/ml and subjected to 6-day exposure of 21% or 50% O_2. PPAT KO cells were collected 7–9 days after infection. Equal number of cells from 4 independent biological replicates were collected. Lung tissues were harvested from C57BL/6J mice exposed to room air or 80% O_2 for 5 days. Samples were flash frozen in liquid nitrogen.

Metabolomics was performed by MsOmics (Vedbaek, Copenhagen). The samples were split equally and dried under nitrogen flow for the measurements of polar and semi-polar metabolites. The analysis was performed using a Thermo Scientific Vanquish LC coupled to Thermo Q Enactive HF MS. The metabolites were ionized by an electrospray ionization interface. The data were acquired from both positive and negative ion modes. UPLC for polar and semi-polar metabolites was carried out using protocols slightly modified from Hsiao et al. and Doneunu et al., respectively [71,110]. Peak areas were annotated and quantified using Compound Discoverer 3.1 (Thermo Scientific).

Comet cellular DNA damage—Dummy and ERCC2 KO cells were generated from K562 cells with the sgRNA sequences listed in Table S6. As a positive control, K562 cells

were exposed to UV light for 1hr in a cell culture hood. Male WT mice (n=3 each condition) were exposed to 21% or 80% O_2 for 5 days. Mice were sacrificed following isoflurane anesthesia. Single cells from the lung were isolated from the lungs as described previously [111]. The cell pellet was resuspended in ice cold PBS for the comet assay.

Cellular DNA damage was measured by the comet assay in alkaline solution (Abcam 238544) according to the manufacturer's instructions. The slides for *in vitro* and *in vivo* samples were imaged with a Nikon Spinning Disk epifluorescent microscope and a Zeiss Observer Z1 inverted fluorescent microscope, respectively. At least 35 randomly selected nucleoids were analyzed per in vitro sample and at least 150 nucleoids were analyzed per mouse sample using Comet Score 2.0 software. Data are presented as percent of DNA in the comet tail; the intensity of the comet tail relative to the comet nucleoid head indicates the extent of DNA damage, including DNA single- and double-strand breaks, alkali labile DNA adducts, and the majority of apurinic/apyrimidinic sites. The experiment was performed in 3 independent biological replicates.

Nucleotide excision repair (NER) efficiency—The NER efficiency assay was modified from the host cell reactivation assay [79]. The pGL3 vector (Promega E1751) was diluted in sterile water and subjected to various degrees of UV irradiation (0–7500 μJ/cm^2 x100) to induce DNA damage using the Stratalinker UV Crosslinker Model 2400 (265-nm UV light bulb). 200ng of DNA was amplified by PCR (Ex Taq DNA polymerase, Takara Bio) and run on an 1% agarose gel to verify UV-induced damage of the plasmid. The vector irradiated at 1500 μJ/cm^2 X 100 was used for the following experiments.

K562 cells (Dummy under 21% O_2, Dummy under 6 days 50% O_2 exposure, and sgERCC2 under 21% O_2) were transfected in 6-well plates. On the day of transfection, cells (5 $x10^5$) were plated in growth medium without antibiotics. 4.5 μg of the pGL3 reporter vector and 0.5 μg of the pSV β-galactosidase vector (Promega E1081) were mixed with 500 μL Opti-MEM I reduced serum media (Life Technologies, #31985062). Undamaged pGL3 plasmid DNA was used as a positive control for each sample. The PLUS reagent (Thermo Fisher 15338100, 5 μL) was added, and the resulting mixture was incubated for 10min at RT. For each well of cells, Lipofectamine LTX (Thermo Fisher 15338100, 13.75 μL) was added into the diluted DNA solution and the mixture was incubated at RT for 25min to form DNA-lipofectamine LTX complexes. The resulting complexes were added to each well. Cells were incubated at 37°C for 48 hours post-transfection.

Cell pellets were resuspended in 1X Reporter Lysis Buffer (Promega E4030). The luciferase activities were quantified according to the manufacturer's instructions. To quantify the expression of β-galactosidase, the cell lysates were mixed with breaking buffer (0.2 M Tris-HCl, 0.2 M NaCl, 0.01 M Mg acetate, 0.01 M 2-mercaptoethanol, 5% glycerol, pH 7.6), Z buffer (0.06 M Na_2HPO_4, 0.04 M NaH_2PO_4, 0.01 M KCl, 0.001 M $MgSO_4$, 0.05 M 2-mercaptoethanol, pH 7.0) and 4 mg/mL o-Nitrophenyl-β-D-galactosidase (ONPG) in milli-Q H_2O as previously described [79]. The resulting mixtures were incubated at 28°C until the solution turned visibly yellow. The absorbance was measured at 420nm at the same time for all samples. The experiment was performed in 3 independent biological replicates.

To calculate the relative transcription-coupled repair (TCR) capacities, the luciferase RLU was divided by the β-galactosidase expression to correct for transfection efficiency. TCR was quantified by dividing TCR capacities of damaged wells to undamaged wells.

Mitochondrial respiration of K562 cells—K562 cells were exposed to 21% or 50% O_2 for 2, 4 and 6 days. Cell-Tak (25 μg/mL) was added to the Seahorse XFe96 Cell Culture Plates to optimize cell adherence. Prior to the assay, 1.20 x 10^5 cells were plated per well. The plates were centrifuged at 600g for 5min at 4°C. The assay media was composed of DMEM Powder (Sigma, D5030), 5mM HEPES, 30 mM NaCl, 0.3 mg/L Phenol Red, 8 mM glucose, 2 mM pyruvate and 0.2 mM glutamine (pH 7.4). Port A of the Seahorse XFe96 Sensor Cartridges was loaded with oligomycin (final conc. = 1.5 μM). Both ports B and C were loaded with FCCP (final conc. = 0.6 μM). Port D was loaded with piericidin A and antimycin A (final conc. = 1 μM for both). The experiment was performed in 3 biological replicates and 10 technical replicates.

Basal and maximal respiration were calculated by subtracting piericidin/antimycin-insensitive respiration:

$$BasalOCR = average(OCR_{Baseline}) - min(OCR_{(Piericidin\ +\ Antimycin)})$$

$$MaximalOCR = max(OCR_{FCCP}) - min(OCR_{(Piericidin\ +\ Antimycin)})$$

qPCR—RNA was extracted from K562 cells with TRIzol Reagent (Thermo Fisher, 15596026) or RNeasy Mini Kit (Qiagen, 74104), and was reverse transcribed using the QuantiTect Reverse Transcription Kit (Qiagen, 205311) according to the manufacturer's instructions. The qPCR reactions were performed using gene-specific qPCR primers (Table S6C) and Maxima SYBR Green/ROX qPCR Master Mix (Thermo Fisher, K02222) on the QuantStudio 5 real-time PCR machine (Applied Biosystems). Relative gene expression was calculated using the delta-delta Ct method. Expression of all genes was normalized to expression of the housekeeping gene, HPRT1. The experiments were performed in 3 biological replicates and 3 technical replicates.

Protein depletion mechanisms—For the cycloheximide (CHX) assay, cells were treated with 50 μg/ml CHX (Neta Scientific, RPI-C81040–1.0) for 0, 1, 2, or 3 days at 37°C under 21% or 50% O_2. For the proteasome and autophagy inhibition experiments, to avoid cell toxicity, cells were pretreated with different O_2 tensions prior to the drug treatment. More specifically, cells were first exposed to 21% or 50% O_2 for 36hr and then treated with bortezomib (Sigma-Aldrich 5043140001) or Bafliomycin A1 (Sigma-Aldrich 19–148) under respective oxygen tensions for 12hr.

For the inducible CRISPRi experiments, cell lines with Dummy or sgRNAs were pre-treated with to 100 nM doxycycline for 48hr. Subsets of cells were harvested for qPCR to validate KD. The rest of cells were replated and subjected to 21% or 50% O_2 for 72hr. The concertation of doxycycline was adjusted to 100 nM daily assuming a half-life of 24hr.

Lung pathology—Age-matched male C57Bl/6 mice were exposed to room air (21% O_2) or hyperoxia (80% O_2). Mice (n = 3 for each condition) were euthanized by CO_2 inhalation followed by cervical dislocation. Ndufs4 KO and control mice were exposed to 50% O2 for 48 hours. The lungs were perfused via the right ventricle with ice cold PBS for 2 minutes. The lungs were inflated with 1ml of 4% PFA. The lung tissues were fixed in 4% paraformaldehyde (Thermo Fisher, 50–980-495) at 4C overnight, washed with ice cold PBS, and then placed in 30% sucrose solution at 4°C for 2–3 days. The lung tissues were blocked in OCT and frozen immediately at −80°C. H&E staining was performed by the Core Histology Facility at Gladstone Institutes (San Francisco, CA, USA) or UCSF Histology Core (San Francisco, CA, USA).

Evans blue dye extravasation—Mice were anesthetized with isoflurane. 50μL of Evans blue dye (30mg/ml in 0.9% normal saline; Sigma-Aldrich E2129) was injected into the retro-orbital sinus. The mice were sedated for 20 minutes under isoflurane. Mice were then sacrificed. The lungs were perfused via the right ventricle with ice-cold PBS for 1 minute. The entire right lung was carefully removed and weighed. The entire left lung was carefully removed and weighed, then flash frozen in liquid nitrogen. The right lung was placed in heat block at 60C for 24 hours and re-weighed to obtain the dry weight and to calculate the wet:dry ratio. In order to quantify the Evans blue dye from the left lung, 250μL of formamide was added to the lung and placed in an orbital shaker, 300 rpm at 30°C overnight. The tubes were centrifuged at 5000g x 10 minutes and the supernatant was removed. The supernatant was quantified using a 96 well microplate, absorbance OD620 nm.

Lung immunofluorescence—Age-matched male C57Bl/6 mice exposed to room air (21% O_2) or hyperoxia (80% O_2) were euthanized by isoflurane followed by cervical dislocation (n = 3 for each condition). Lung tissues were perfused with ice-old PBS for 1 min, followed by 4% paraformaldehyde in PBS for 1min. Lung tissues were inflated with 1mL 4% paraformaldehyde, and immersed in 4% paraformaldehyde for 1 hr at room temperature. Lung tissues were then washed with ice-cold PBS twice, and coated with 30% sucrose in PBS for 5 min. The tissues were injected with 1mL of OCT each, mounted in OCT, and frozen at −80°C. Tissue were cut at 10 μm per section using a cryostat.

Tissue slides were immersed in pre-heated R&D System Antigen Retrieval Reagent Basic (R&D System 950510) for 20 min in a Coplin jar in a water bath at 95°C for antigen retrieval. Following wash with PBS, slides were incubated in in permeabilization buffer (1% donkey serum, 0.1% Triton X-100 in PBS) for 10 min, and blocked with blocking buffer (1% BSA, 5% donkey serum in PBS) for 1 hr at room temperature. Tissue sections were incubated with primary antibodies (Table S6) in the incubation buffer (1% BSA, 1% donkey serum, and 0.01% sodium azide in PBS) overnight at 4°C in a dark humidified chamber, and secondary antibodies (Table S6) in the incubation buffer for 1 hr at RT in the dark. To minimize the background, the sections were bathed with 1X TrueBlack® Lipofuscin (Biotium 23007) for few seconds. Tissue sections were mounted with an anti-fade mounting media (Vector Laboratories H-1200). Staining were visualized using a fluorescence microscope.

Lung tissue PO_2 measurement—Male C57Bl/6 mice were exposed to normoxia (21% O_2) or hyperoxia (80% O_2 for 3 or 5 days). Male and female *Ndufs4* KO and control mice were exposed only to normoxia, and experiments performed at p35–40. Mice from different groups were randomized at the time of lung tissue PO_2 measurements. Mice were anesthetized with isoflurane (induction at 2–4%, maintenance at 0.5–2%) and placed on an intubation platform (Kent Scientific). Mice were endotracheally intubated, moved to a flat surface, and mechanically ventilated with the MiniVent Type 845 (Hugo Sachs Electronik, Harvard Apparatus). The stroke volume was set to 250μL and the ventilation rate was set to 150 strokes/min. The FiO_2 was set to 1.0 (100% O_2) at time of intubation. Once successful intubation and adequate sedation were verified, FiO_2 was reduced to 0.8. Left thoracotomy was performed to expose the lower portion of the left lung. Lung PO_2 levels were measured with a 100μm-diameter PO_2 probe (Unisense OX-100–011893, Denmark). The probe was polarized for at least 2 hours prior to the experiments. The probe was calibrated in anoxic solution (0mmHg) and atmospheric O_2 solution (160mmHg), and measurements were obtained in mV. The probe was positioned in a micromanipulator and inserted into the left lower lobe. Measurements were obtained with the mice ventilated at different FiO_2 targets (0.3 – 0.8). Each measurement was recorded after the reading was stable for 30 seconds. During each measurement, the depth of anesthesia was reduced by lowering the isoflurane concentration to 0.5–1% to minimize the impact of anesthesia on lung PO_2. The mice were sacrificed following the experiment.

ETC activity in lung tissues—C57Bl/6 mice were housed in normoxia (21%) or hyperoxia (80%) (n = 3 for each treatment group). Mice were euthanized with isoflurane and cervical dislocation. Lung tissues were immediately harvested and placed on ice. Mitochondria were isolated from lung tissues within 1.5 hours of lung tissue harvest. Mitochondrial isolation buffer (MSHE) was composed of 70 mM sucrose, 210 mM mannitol, 5 mM HEPES, 1 mM EGTA and 0.5% (w/v) fatty acid-free BSA (pH 7.2). Tissues were homogenized with Dounce cell homogenizer. The nuclear fraction was removed following centrifugation at 1,000g for 10min at 4°C. To isolate mitochondria, tissue lysate was centrifuged at 20,000g for 10min at 4°C. The isolated mitochondria were resuspended with MSHE and the protein concentration was quantified using the Pierce™ Rapid Gold BCA protein assay kit (Thermo Scientific A53225).

Enzymatic activities of mitochondrial ETC Complexes I, II and IV were measured using the Seahorse XF96 Analyzer. Equal amounts of mitochondria (7.5μg) were plated on Seahorse cell culture plates. Plates were centrifuged at 2,000g for 10min at 4°C. The assay media was composed of 1 X MAS buffer (70 mM sucrose, 220mM mannitol, 10 mM KH_2PO_4, 5 mM $MgCl_2$, 2mM HEPES and 1 mM EGTA), 10μg/mL Cytochrome c and 10μg/mL alamethicin (pH 7.4). The assay media was pre-warmed at 37°C and added to the culture plate prior to the assay. To measure the activity of ETC Complex I, Port A of the Seahorse XFe96 sensor cartridge was loaded with NADH (final concentration = 1.43 mM). To measure the activity of ETC Complex II, Port A of the cartridge was loaded with succinate (final concentration = 1.43 mM) and piericidin A (final concentration = 0.29 mM). Port B was loaded with piericidin A (final concentration = 2.5 μM) and antimycin A (final concentration = 5.0 μM). To measure Complex IV activity, Port C was loaded with ascorbic acid (final concentration

= 1.11 mM) and N ,N,N′,N′-tetramethyl-p-phenylenediamine (TMPD, final concentration = 0.56 mM). Port D was loaded with azide (final concentration = 50 mM). Each sample had 5 technical replicates. Oxygen consumption rates (OCR) were measured 3 times following each injection.

Enzymatic activities of Complexes I and II were calculated by subtracting the minimal OCR following the injection of azide, from the maximal OCR following the injections of the respective substrates.

$$Complex\ I\ Activity = \max(OCR_{NADH}) - \min(OCR_{Azide})$$

$$Complex\ II\ Activity = \max(OCR_{Succinate\ +\ Piericidin}) - \min(OCR_{Azide})$$

QUANTIFICATION AND STATISTICAL ANALYSIS

CRISPR screen analysis—First, raw sequencing reads from next-generation sequencing were aligned and quantified using the MAGeCK algorithm [47]. Second, the data were analyzed using a maximum likelihood estimate (MAGeCK-MLE) to compute the gene essentiality under perturbation (50% O_2) and control (21% O_2) conditions [112]. We used MAGeCK-MLE to model both conditions and passage numbers to estimate the effects of perturbation and control on sgRNA abundance as beta scores. To account for different proliferation rates under two conditions, we normalized the beta scores with a list of 625 core essential genes [47]. The genes were ranked based on differential gene essentiality ($\Delta\ \beta = \beta_{Hyperoxia} - \beta_{Normoxia}$). Genes with $\Delta\ \beta > average(\Delta\ \beta) + 2 \times SD(\Delta\ \beta)$ were considered “buffering genes”. Genes with $\Delta\ \beta < average(\Delta\ \beta) - 2 \times SD(\Delta\ \beta)$ were considered “sensitizing genes”. Pathway enrichment analysis was performed using the ‘EnrichAnalyzer’ function and the hypergeometric test in the R package MAGeCKFlute [47]. Buffering and sensitizing genes were mapped against the Gene Ontology database[113].

TMT proteomics data analysis—For the TMT proteomics, the mass spectra were analyzed with MaxQuant software (1.5.5.1). MS/MS spectra were annotated using the UniProt protein sequence database and GPM cRAP sequences (retrieved in January 2020). The mass tolerance for the precursor mass and product ions was set to 4.5ppm and 0.5 Da, respectively. The maximum precursor ion charge state was set to 7. The cutoff for the target-decoy-based false discovery rate (FDR) was set to 1% to filter spectrum and protein with low confidence.

The protein abundance was median normalized and was $\log_2$-transformed to stabilize the variance. Next, the means for each protein were compared with unpaired t-test (Python SciPy v1.5.0) and the adjusted p-values were computed with the Benjamini-Hochberg method (Python statmodels v0.12.2).

DIA proteomics data analysis—For the label-free proteomics in mouse lung tissues, raw files were processed with SpectronautTM (Biognosys, v14.9.201124.47784) software

using directDIA mode against curated mouse Uniprot proteome without isoforms (17,027 entries, retrieved in January 2020) with standard setting with some modifications. IDPicker algorithm was picked for protein inference.

Spectronaut-obtained feature intensities were log_2-transformed and loess-normalized to account for systematic errors. Differential expression analysis was performed using unpaired t-test (Python SciPy v1.5.0).

Metabolomics data analysis—The abundance of metabolites in K562 cells was normalized by cell count. A total of 476 unique metabolites were quantified in cells. If same metabolites were detected following polar and semi-polar extraction methods, the results with higher means across all samples were used for downstream analyses. For lung metabolomics, a total of 158 metabolites were quantified. The normalized abundance was log_2-transformed. The means for each metabolite across conditions were compared with unpaired t-test and the adjusted p-values were computed with the Benjamini-Hochberg method.

For the PCA analysis, the normalized metabolite abundance was scaled and the PCA was performed using the Scikit-learn package (v0.24.1) in Python. The number of dimensions was set to 3. Enrichment analysis was performed with the MetaboAnalyst 5.0 web server [114]. The metabolites that were significantly enriched or depleted in both Dummy 50% O_2 and sgPPAT were compared to the KEGG database using the overrepresentation test.

CRISPR screen comparisons—The top 500 buffering genes in our hyperoxia genome-wide CRISPR KO screen were compared to the top 500 buffering genes from the previously published genome-wide CRISPR KO screens with hydrogen peroxide [84] and ETC inhibitors [83]. The hypergeometric test was performed to compare enrichment of the four pathways. The similarity of the top buffering genes across different perturbations was represented by the Jaccard index (the size of the intersection divided by that of the union of two gene sets), as well as the number of overlapping genes.

Statistical analysis for functional assays—Data from the functional assays are reported as mean +/− SEM. All the comparisons between two groups were analyzed using the unpaired t-test with Welch's correction. Comparisons of multiple groups were performed with Tukey's multiple comparisons. The analyses and plots were generated using GraphPad Prism 9. P-values less than 0.05 were considered statistically significant.

Supplementary Material

Refer to Web version on PubMed Central for supplementary material.

Acknowledgments

We thank Guo Huang, Dengke Ma, Andy Chang, and Emily Goldberg for discussions. We thank Xiaoxin Chen, James Jung, Xiaohui Fang, and Christopher Molina for technical assistance. We thank Francoise Chanut, Bruce Conklin and Benoit Bruneau for reviewing the manuscript. We acknowledge Gladstone Histology Core, UCSF Center for Advanced Technology, and MsOmics for technical assistance. AHB was supported by T32-HL007731, Chan-Zuckerberg Biohub Physician-Scientist Fellowship, and Sarnoff Scholar Award. IHJ was supported by NIH

DP5 DP5OD026398. This work was supported by NIH DP5OD026398 and UCSF Program for Breakthrough Biomedical Research (PBBR).

REFERENCES:

1. Hodgskiss MSW, Crockford PW, Peng Y, Wing BA, and Horner TJ (2019). A productivity collapse to end Earth's Great Oxidation. Proc Natl Acad Sci USA 116, 17207–17212. 10.1073/pnas.1900325116. [PubMed: 31405980]
2. Lyons TW, Reinhard CT, and Planavsky NJ (2014). The rise of oxygen in Earth's early ocean and atmosphere. Nature 506, 307–315. 10.1038/nature13068. [PubMed: 24553238]
3. Friedman ES, Bittinger K, Esipova TV, Hou L, Chau L, Jiang J, Mesaros C, Lund PJ, Liang X, FitzGerald GA, et al. (2018). Microbes vs. chemistry in the origin of the anaerobic gut lumen. Proc Natl Acad Sci U S A 115, 4170–4175. 10.1073/pnas.1718635115. [PubMed: 29610310]
4. Stewart FJ, Newton ILG, and Cavanaugh CM (2005). Chemosynthetic endosymbioses: adaptations to oxic-anoxic interfaces. Trends Microbiol 13, 439–448. 10.1016/j.tim.2005.07.007. [PubMed: 16054816]
5. Griffith OW (1999). Biologic and pharmacologic regulation of mammalian glutathione synthesis. Free Radic Biol Med 27, 922–935. 10.1016/s0891-5849(99)00176-8. [PubMed: 10569625]
6. Warner HR (1994). Superoxide dismutase, aging, and degenerative disease. Free Radic Biol Med 17, 249–258. 10.1016/0891-5849(94)90080-9. [PubMed: 7982630]
7. Harrison JF, Kaiser A, and VandenBrooks JM (2010). Atmospheric oxygen level and the evolution of insect body size. Proc Biol Sci 277, 1937–1946. 10.1098/rspb.2010.0001. [PubMed: 20219733]
8. Hetz SK, and Bradley TJ (2005). Insects breathe discontinuously to avoid oxygen toxicity. Nature 433, 516–519. 10.1038/nature03106. [PubMed: 15690040]
9. Epstein AC, Gleadle JM, McNeill LA, Hewitson KS, O'Rourke J, Mole DR, Mukherji M, Metzen E, Wilson MI, Dhanda A, et al. (2001). C. elegans EGL-9 and mammalian homologs define a family of dioxygenases that regulate HIF by prolyl hydroxylation. Cell 107, 43–54. 10.1016/s0092-8674(01)00507-4. [PubMed: 11595184]
10. Ivan M, Kondo K, Yang H, Kim W, Valiando J, Ohh M, Salic A, Asara JM, Lane WS, and Kaelin WG (2001). HIFalpha targeted for VHL-mediated destruction by proline hydroxylation: implications for O2 sensing. Science 292, 464–468. 10.1126/science.1059817. [PubMed: 11292862]
11. Semenza GL, Nejfelt MK, Chi SM, and Antonarakis SE (1991). Hypoxia-inducible nuclear factors bind to an enhancer element located 3' to the human erythropoietin gene. Proc Natl Acad Sci U S A 88, 5680–5684. 10.1073/pnas.88.13.5680. [PubMed: 2062846]
12. Wang GL, Jiang BH, Rue EA, and Semenza GL (1995). Hypoxia-inducible factor 1 is a basic-helix-loop-helix-PAS heterodimer regulated by cellular O2 tension. Proc Natl Acad Sci U S A 92, 5510–5514. 10.1073/pnas.92.12.5510. [PubMed: 7539918]
13. Caldwell J (1965). Effects of high partial pressures of oxygen on fungi and bacteria. Nature 206, 321–323. 10.1038/206321a0. [PubMed: 5836342]
14. Caldwell J (1964). EFFECT OF HIGH PRESSURES OF PURE OXYGEN ON TISSUES. Nature 201, 514–515. 10.1038/201514a0. [PubMed: 14164640]
15. Boehm DE, Vincent K, and Brown OR (1976). Oxygen and toxicity inhibition of amino acid biosynthesis. Nature 262, 418–420. 10.1038/262418a0. [PubMed: 785275]
16. Gregory EM, Goscin SA, and Fridovich I (1974). Superoxide dismutase and oxygen toxicity in a eukaryote. J Bacteriol 117, 456–460. 10.1128/JB.117.2.456-460.1974. [PubMed: 4590469]
17. Haugaard N (1968). Cellular mechanisms of oxygen toxicity. Physiol Rev 48, 311–373. 10.1152/physrev.1968.48.2.311. [PubMed: 4870377]
18. Brugniaux JV, Coombs GB, Barak OF, Dujic Z, Sekhon MS, and Ainslie PN (2018). Highs and lows of hyperoxia: physiological, performance, and clinical aspects. Am J Physiol Regul Integr Comp Physiol 315, R1–R27. 10.1152/ajpregu.00165.2017. [PubMed: 29488785]
19. Donald KW (1947). Oxygen poisoning in man. Br Med J 1, 667; passim. [PubMed: 20248086]
20. Angus DC (2020). Oxygen Therapy for the Critically Ill. N Engl J Med 382, 1054–1056. 10.1056/NEJMe2000800. [PubMed: 32160668]

21. Chu DK, Kim LH-Y, Young PJ, Zamiri N, Almenawer SA, Jaeschke R, Szczeklik W, Schünemann HJ, Neary JD, and Alhazzani W (2018). Mortality and morbidity in acutely ill adults treated with liberal versus conservative oxygen therapy (IOTA): a systematic review and meta-analysis. The Lancet 391, 1693–1705. 10.1016/S0140-6736(18)30479-3.
22. Principi N, Di Pietro GM, and Esposito S (2018). Bronchopulmonary dysplasia: clinical aspects and preventive and therapeutic strategies. J Transl Med 16, 36. 10.1186/s12967-018-1417-7. [PubMed: 29463286]
23. Watterberg KL, Walsh MC, Li L, Chawla S, D'Angio CT, Goldberg RN, Hintz SR, Laughon MM, Yoder BA, Kennedy KA, et al. (2022). Hydrocortisone to Improve Survival without Bronchopulmonary Dysplasia. N Engl J Med 386, 1121–1131. 10.1056/NEJMoa2114897. [PubMed: 35320643]
24. Hellström A, Smith LEH, and Dammann O (2013). Retinopathy of prematurity. Lancet 382, 1445–1457. 10.1016/S0140-6736(13)60178-6. [PubMed: 23782686]
25. Higgins RD (2019). Oxygen Saturation and Retinopathy of Prematurity. Clin Perinatol 46, 593–599. 10.1016/j.clp.2019.05.008. [PubMed: 31345549]
26. Barrot L, Asfar P, Mauny F, Winiszewski H, Montini F, Badie J, Quenot J-P, Pili-Floury S, Bouhemad B, Louis G, et al. (2020). Liberal or Conservative Oxygen Therapy for Acute Respiratory Distress Syndrome. N Engl J Med 382, 999–1008. 10.1056/NEJMoa1916431. [PubMed: 32160661]
27. Daher A, Balfanz P, Aetou M, Hartmann B, Müller-Wieland D, Müller T, Marx N, Dreher M, and Cornelissen CG (2021). Clinical course of COVID-19 patients needing supplemental oxygen outside the intensive care unit. Sci Rep 11, 2256. 10.1038/s41598-021-81444-9. [PubMed: 33500431]
28. Guensch DP, Fischer K, Yamaji K, Luescher S, Ueki Y, Jung B, Erdoes G, Gräni C, von Tengg-Kobligk H, Räber L, et al. (2020). Effect of Hyperoxia on Myocardial Oxygenation and Function in Patients With Stable Multivessel Coronary Artery Disease. J Am Heart Assoc 9, e014739. 10.1161/JAHA.119.014739. [PubMed: 32089047]
29. Stub D, Smith K, Bernard S, Nehme Z, Stephenson M, Bray JE, Cameron P, Barger B, Ellims AH, Taylor AJ, et al. (2015). Air Versus Oxygen in ST-Segment-Elevation Myocardial Infarction. Circulation 131, 2143–2150. 10.1161/CIRCULATIONAHA.114.014494. [PubMed: 26002889]
30. Girardis M, Busani S, Damiani E, Donati A, Rinaldi L, Marudi A, Morelli A, Antonelli M, and Singer M (2016). Effect of Conservative vs Conventional Oxygen Therapy on Mortality Among Patients in an Intensive Care Unit: The Oxygen-ICU Randomized Clinical Trial. JAMA 316, 1583–1589. 10.1001/jama.2016.11993. [PubMed: 27706466]
31. Ni Y-N, Wang Y-M, Liang B-M, and Liang Z-A (2019). The effect of hyperoxia on mortality in critically ill patients: a systematic review and meta analysis. BMC Pulm Med 19, 53. 10.1186/s12890-019-0810-1. [PubMed: 30808337]
32. Damiani E, Adrario E, Girardis M, Romano R, Pelaia P, Singer M, and Donati A (2014). Arterial hyperoxia and mortality in critically ill patients: a systematic review and meta-analysis. Crit Care 18, 711. 10.1186/s13054-014-0711-x. [PubMed: 25532567]
33. Bonsignore MR, Esquinas C, Barceló A, Sanchez-de-la-Torre M, Paternó A, Duran-Cantolla J, Marín JM, and Barbé F (2012). Metabolic syndrome, insulin resistance and sleepiness in real-life obstructive sleep apnoea. Eur Respir J 39, 1136–1143. 10.1183/09031936.00151110. [PubMed: 22075482]
34. Chouchani ET, Pell VR, Gaude E, Aksentijević D, Sundier SY, Robb EL, Logan A, Nadtochiy SM, Ord ENJ, Smith AC, et al. (2014). Ischaemic accumulation of succinate controls reperfusion injury through mitochondrial ROS. Nature 515, 431–435. 10.1038/nature13909. [PubMed: 25383517]
35. Jain IH, Zazzeron L, Goldberger O, Marutani E, Wojtkiewicz GR, Ast T, Wang H, Schleifer G, Stepanova A, Brepoels K, et al. (2019). Leigh Syndrome Mouse Model Can Be Rescued by Interventions that Normalize Brain Hyperoxia, but Not HIF Activation. Cell Metab 30, 824–832.e3. 10.1016/j.cmet.2019.07.006. [PubMed: 31402314]
36. Jain IH, Zazzeron L, Goli R, Alexa K, Schatzman-Bone S, Dhillon H, Goldberger O, Peng J, Shalem O, Sanjana NE, et al. (2016). Hypoxia as a therapy for mitochondrial disease. Science 352, 54–61. 10.1126/science.aad9642. [PubMed: 26917594]

37. Hayatdavoudi G, O'Neil JJ, Barry BE, Freeman BA, and Crapo JD (1981). Pulmonary injury in rats following continuous exposure to 60% O2 for 7 days. J Appl Physiol Respir Environ Exerc Physiol 51, 1220–1231. 10.1152/jappl.1981.51.5.1220. [PubMed: 6457819]
38. Crapo JD, DeLong DM, Sjostrom K, Hasler GR, and Drew RT (1977). The failure of aerosolized superoxide dismutase to modify pulmonary oxygen toxicity. Am Rev Respir Dis 115, 1027–1033. 10.1164/arrd.1977.115.6.1027. [PubMed: 262097]
39. Folz RJ, Abushamaa AM, and Suliman HB (1999). Extracellular superoxide dismutase in the airways of transgenic mice reduces inflammation and attenuates lung toxicity following hyperoxia. J Clin Invest 103, 1055–1066. 10.1172/JCI3816. [PubMed: 10194479]
40. Ho YS, Vincent R, Dey MS, Slot JW, and Crapo JD (1998). Transgenic models for the study of lung antioxidant defense: enhanced manganese-containing superoxide dismutase activity gives partial protection to B6C3 hybrid mice exposed to hyperoxia. Am J Respir Cell Mol Biol 18, 538–547. 10.1165/ajrcmb.18.4.2959. [PubMed: 9533942]
41. Kiskurno S, Ryan RM, Paturi B, Wang H, and Kumar VH (2020). Antioxidant MnTBAP does not protect adult mice from neonatal hyperoxic lung injury. Respir Physiol Neurobiol 282, 103545. 10.1016/j.resp.2020.103545. [PubMed: 32927098]
42. Paturi B, Ryan RM, Nielsen L, Wang H, and Kumar VHS (2021). Effects of antioxidant MnTBAP on angiogenesis in newborn mice with hyperoxic lung injury. J Neonatal Perinatal Med 14, 53–60. 10.3233/NPM-200483. [PubMed: 32804105]
43. Griffith DE, Garcia JGN, James HL, Callahan KS, Iriana S, and Holiday D (1992). Hyperoxic Exposure in Humans. Chest 101, 392–397. 10.1378/chest.101.2.392. [PubMed: 1310457]
44. Baik AH, and Jain IH (2020). Turning the Oxygen Dial: Balancing the Highs and Lows. Trends in Cell Biology 30, 516–536. 10.1016/j.tcb.2020.04.005. [PubMed: 32386878]
45. Jain IH, Calvo SE, Markhand AL, Skinner OS, To T-L, Ast T, and Mootha VK (2020). Genetic Screen for Cell Fitness in High or Low Oxygen Highlights Mitochondrial and Lipid Metabolism. Cell 181, 1–12. [PubMed: 32243785]
46. Doench JG, Fusi N, Sullender M, Hegde M, Vaimberg EW, Donovan KF, Smith I, Tothova Z, Wilen C, Orchard R, et al. (2016). Optimized sgRNA design to maximize activity and minimize off-target effects of CRISPR-Cas9. Nat Biotechnol 34, 184–191. 10.1038/nbt.3437. [PubMed: 26780180]
47. Wang B, Wang M, Zhang W, Xiao T, Chen C-H, Wu A, Wu F, Traugh N, Wang X, Li Z, et al. (2019). Integrative analysis of pooled CRISPR genetic screens using MAGeCKFlute. Nat Protoc 14, 756–780. 10.1038/s41596-018-0113-7. [PubMed: 30710114]
48. Zhang Y, Zhu X, Torelli AT, Lee M, Dzikovski B, Koralewski RM, Wang E, Freed J, Krebs C, Ealick SE, et al. (2010). Diphthamide biosynthesis requires an organic radical generated by an iron-sulphur enzyme. Nature 465, 891–896. 10.1038/nature09138. [PubMed: 20559380]
49. Andreini C, Rosato A, and Banci L (2017). The Relationship between Environmental Dioxygen and Iron-Sulfur Proteins Explored at the Genome Level. PLoS One 12, e0171279. 10.1371/journal.pone.0171279. [PubMed: 28135316]
50. Bruska MK, Stiebritz MT, and Reiher M (2013). Analysis of differences in oxygen sensitivity of Fe-S clusters. Dalton Trans 42, 8729–8735. 10.1039/c3dt50763g. [PubMed: 23632881]
51. Glatt S, Zabel R, Kolaj-Robin O, Onuma OF, Baudin F, Graziadei A, Taverniti V, Lin T-Y, Baymann F, Seraphin B, et al. (2016). Structural basis for tRNA modification by Elp3 from Dehalococcoides mccartyi. Nat Struct Mol Biol 23, 794–802. 10.1038/nsmb.3265. [PubMed: 27455459]
52. Quirós PM, Langer T, and López-Otín C (2015). New roles for mitochondrial proteases in health, ageing and disease. Nat Rev Mol Cell Biol 16, 345–359. 10.1038/nrm3984. [PubMed: 25970558]
53. Chandel NS, and Budinger GRS (2007). The cellular basis for diverse responses to oxygen. Free Radical Biology and Medicine 42, 165–174. 10.1016/j.freeradbiomed.2006.10.048. [PubMed: 17189822]
54. Barber RE, and Hamilton WK (1970). Oxygen toxicity in man. A prospective study in patients with irreversible brain damage. N Engl J Med 283, 1478–1484. 10.1056/NEJM197012312832702. [PubMed: 4921729]

55. Davis WB, Rennard SI, Bitterman PB, and Crystal RG (1983). Pulmonary oxygen toxicity. Early reversible changes in human alveolar structures induced by hyperoxia. N Engl J Med 309, 878–883. 10.1056/NEJM198310133091502. [PubMed: 6888481]
56. Fisher AB, and Beers MF (2008). Hyperoxia and acute lung injury. Am J Physiol Lung Cell Mol Physiol 295, L1066; author reply L1067. 10.1152/ajplung.90486.2008. [PubMed: 19047485]
57. Kallet RH, and Matthay MA (2013). Hyperoxic acute lung injury. Respir Care 58, 123–141. 10.4187/respcare.01963. [PubMed: 23271823]
58. Kapanci Y, Tosco R, Eggermann J, and Gould VE (1972). Oxygen pneumonitis in man., Light- and electron-microscopic morphometric studies. Chest 62, 162–169. 10.1378/chest.62.2.162. [PubMed: 5050222]
59. Matute-Bello G, Frevert CW, and Martin TR (2008). Animal models of acute lung injury. Am J Physiol Lung Cell Mol Physiol 295, L379–399. 10.1152/ajplung.00010.2008. [PubMed: 18621912]
60. Matthay MA, Zemans RL, Zimmerman GA, Arabi YM, Beitler JR, Mercat A, Herridge M, Randolph AG, and Calfee CS (2019). Acute respiratory distress syndrome. Nat Rev Dis Primers 5, 18. 10.1038/s41572-019-0069-0. [PubMed: 30872586]
61. Freeman BA, and Crapo JD (1981). Hyperoxia increases oxygen radical production in rat lungs and lung mitochondria. Journal of Biological Chemistry 256, 10986–10992. 10.1016/S0021-9258(19)68544-3. [PubMed: 7287745]
62. Chen C-M, and Behringer RR (2004). Ovca1 regulates cell proliferation, embryonic development, and tumorigenesis. Genes Dev 18, 320–332. 10.1101/gad.1162204. [PubMed: 14744934]
63. Liu S, Milne GT, Kuremsky JG, Fink GR, and Leppla SH (2004). Identification of the proteins required for biosynthesis of diphthamide, the target of bacterial ADP-ribosylating toxins on translation elongation factor 2. Mol Cell Biol 24, 9487–9497. 10.1128/MCB.24.21.9487-9497.2004. [PubMed: 15485916]
64. Su X, Lin Z, and Lin H (2013). The biosynthesis and biological function of diphthamide. Crit Rev Biochem Mol Biol 48, 515–521. 10.3109/10409238.2013.831023. [PubMed: 23971743]
65. Urreizti R, Mayer K, Evrony GD, Said E, Castilla-Vallmanya L, Cody NAL, Plasencia G, Gelb BD, Grinberg D, Brinkmann U, et al. (2020). DPH1 syndrome: two novel variants and structural and functional analyses of seven missense variants identified in syndromic patients. Eur J Hum Genet 28, 64–75. 10.1038/s41431-019-0374-9. [PubMed: 30877278]
66. Gupta PK, Liu S, Batavia MP, and Leppla SH (2008). The diphthamide modification on elongation factor-2 renders mammalian cells resistant to ricin. Cell Microbiol 10, 1687–1694. 10.1111/j.1462-5822.2008.01159.x. [PubMed: 18460012]
67. Roy V, Ghani K, and Caruso M (2010). A dominant-negative approach that prevents diphthamide formation confers resistance to Pseudomonas exotoxin A and diphtheria toxin. PLoS One 5, e15753. 10.1371/journal.pone.0015753. [PubMed: 21203470]
68. Liu S, Bachran C, Gupta P, Miller-Randolph S, Wang H, Crown D, Zhang Y, Wein AN, Singh R, Fattah R, et al. (2012). Diphthamide modification on eukaryotic elongation factor 2 is needed to assure fidelity of mRNA translation and mouse development. Proc Natl Acad Sci U S A 109, 13817–13822. 10.1073/pnas.1206933109. [PubMed: 22869748]
69. Mouzakis KD, Lang AL, Vander Meulen KA, Easterday PD, and Butcher SE (2013). HIV-1 frameshift efficiency is primarily determined by the stability of base pairs positioned at the mRNA entrance channel of the ribosome. Nucleic Acids Res 41, 1901–1913. 10.1093/nar/gks1254. [PubMed: 23248007]
70. Ducker GS, and Rabinowitz JD (2017). One-Carbon Metabolism in Health and Disease. Cell Metab 25, 27–42. 10.1016/j.cmet.2016.08.009. [PubMed: 27641100]
71. Hsiao JJ, Potter OG, Chu T-W, and Yin H (2018). Improved LC/MS Methods for the Analysis of Metal-Sensitive Analytes Using Medronic Acid as a Mobile Phase Additive. Anal Chem 90, 9457–9464. 10.1021/acs.analchem.8b02100. [PubMed: 29976062]
72. Bohr VA, Smith CA, Okumoto DS, and Hanawalt PC (1985). DNA repair in an active gene: removal of pyrimidine dimers from the DHFR gene of CHO cells is much more efficient than in the genome overall. Cell 40, 359–369. 10.1016/0092-8674(85)90150-3. [PubMed: 3838150]

73. Hanawalt PC, and Spivak G (2008). Transcription-coupled DNA repair: two decades of progress and surprises. Nat Rev Mol Cell Biol 9, 958–970. 10.1038/nrm2549. [PubMed: 19023283]
74. Singh A, Compe E, Le May N, and Egly J-M (2015). TFIIH subunit alterations causing xeroderma pigmentosum and trichothiodystrophy specifically disturb several steps during transcription. Am J Hum Genet 96, 194–207. 10.1016/j.ajhg.2014.12.012. [PubMed: 25620205]
75. Winkler GS, Araújo SJ, Fiedler U, Vermeulen W, Coin F, Egly J-M, Hoeijmakers JHJ, Wood RD, Timmers H. Th.M., and Weeda G (2000). TFIIH with Inactive XPD Helicase Functions in Transcription Initiation but Is Defective in DNA Repair. Journal of Biological Chemistry 275, 4258–4266. 10.1074/jbc.275.6.4258. [PubMed: 10660593]
76. Cacciuttolo MA, Trinh L, Lumpkin JA, and Rao G (1993). Hyperoxia induces DNA damage in mammalian cells. Free Radic Biol Med 14, 267–276. 10.1016/0891-5849(93)90023-n. [PubMed: 8458584]
77. Forsyth NR, Musio A, Vezzoni P, Simpson AHRW, Noble BS, and McWhir J (2006). Physiologic oxygen enhances human embryonic stem cell clonal recovery and reduces chromosomal abnormalities. Cloning Stem Cells 8, 16–23. 10.1089/clo.2006.8.16. [PubMed: 16571074]
78. Roper JM, Mazzatti DJ, Watkins RH, Maniscalco WM, Keng PC, and O'Reilly MA (2004). In vivo exposure to hyperoxia induces DNA damage in a population of alveolar type II epithelial cells. American Journal of Physiology-Lung Cellular and Molecular Physiology 286, L1045–L1054. 10.1152/ajplung.00376.2003. [PubMed: 14729512]
79. Johnson JM, and Latimer JJ (2005). Analysis of DNA repair using transfection-based host cell reactivation. Methods Mol Biol 291, 321–335. 10.1385/1-59259-840-4:321. [PubMed: 15502233]
80. Read AD, Bentley RET, Archer SL, and Dunham-Snary KJ (2021). Mitochondrial iron–sulfur clusters: Structure, function, and an emerging role in vascular biology. Redox Biology 47, 102164. 10.1016/j.redox.2021.102164. [PubMed: 34656823]
81. Wirth C, Brandt U, Hunte C, and Zickermann V (2016). Structure and function of mitochondrial complex I. Biochimica et Biophysica Acta (BBA) - Bioenergetics 1857, 902–914. 10.1016/j.bbabio.2016.02.013. [PubMed: 26921811]
82. Fiedorczuk K, Letts JA, Degliesposti G, Kaszuba K, Skehel M, and Sazanov LA (2016). Atomic structure of the entire mammalian mitochondrial complex I. Nature 538, 406–410. 10.1038/nature19794. [PubMed: 27595392]
83. To T-L, Cuadros AM, Shah H, Hung WHW, Li Y, Kim SH, Rubin DHF, Boe RH, Rath S, Eaton JK, et al. (2019). A Compendium of Genetic Modifiers of Mitochondrial Dysfunction Reveals Intra-organelle Buffering. Cell 179, 1222–1238.e17. 10.1016/j.cell.2019.10.032. [PubMed: 31730859]
84. Dubreuil MM, Morgens DW, Okumoto K, Honsho M, Contrepois K, Lee-McMullen B, Traber GM, Sood RS, Dixon SJ, Snyder MP, et al. (2020). Systematic Identification of Regulators of Oxidative Stress Reveals Non-canonical Roles for Peroxisomal Import and the Pentose Phosphate Pathway. Cell Rep 30, 1417–1433.e7. 10.1016/j.celrep.2020.01.013. [PubMed: 32023459]
85. Chang S, Kwon N, Kim J, Kohmura Y, Ishikawa T, Rhee CK, Je JH, and Tsuda A (2015). Synchrotron X-ray imaging of pulmonary alveoli in respiration in live intact mice. Sci Rep 5, 8760. 10.1038/srep08760. [PubMed: 25737245]
86. Ferrari M, Jain IH, Goldberger O, Rezoagli E, Thoonen R, Cheng K-H, Sosnovik DE, Scherrer-Crosbie M, Mootha VK, and Zapol WM (2017). Hypoxia treatment reverses neurodegenerative disease in a mouse model of Leigh syndrome. Proc. Natl. Acad. Sci. U.S.A 114, E4241–E4250. 10.1073/pnas.1621511114. [PubMed: 28483998]
87. Taivassalo T, Abbott A, Wyrick P, and Haller RG (2002). Venous oxygen levels during aerobic forearm exercise: An index of impaired oxidative metabolism in mitochondrial myopathy. Ann. Neurol 51, 38–44. 10.1002/ana.10027. [PubMed: 11782982]
88. Chen H, Li X, and Epstein PN (2005). MnSOD and catalase transgenes demonstrate that protection of islets from oxidative stress does not alter cytokine toxicity. Diabetes 54, 1437–1446. 10.2337/diabetes.54.5.1437. [PubMed: 15855331]
89. Qi W, and Cowan JA (2011). Structural, Mechanistic and Coordination Chemistry of Relevance to the Biosynthesis of Iron-Sulfur and Related Iron Cofactors. Coord Chem Rev 255, 688–699. 10.1016/j.ccr.2010.10.016. [PubMed: 21499539]

90. Guarás A, Perales-Clemente E, Calvo E, Acín-Pérez R, Loureiro-Lopez M, Pujol C, Martínez-Carrascoso I, Nuñez E, García-Marqués F, Rodríguez-Hernández MA, et al. (2016). The CoQH2/CoQ Ratio Serves as a Sensor of Respiratory Chain Efficiency. Cell Rep 15, 197–209. 10.1016/j.celrep.2016.03.009. [PubMed: 27052170]

91. Boyd ES, Thomas KM, Dai Y, Boyd JM, and Outten FW (2014). Interplay between oxygen and Fe-S cluster biogenesis: insights from the Suf pathway. Biochemistry 53, 5834–5847. 10.1021/bi500488r. [PubMed: 25153801]

92. Yuvaniyama P, Agar JN, Cash VL, Johnson MK, and Dean DR (2000). NifS-directed assembly of a transient [2Fe-2S] cluster within the NifU protein. Proc Natl Acad Sci U S A 97, 599–604. 10.1073/pnas.97.2.599. [PubMed: 10639125]

93. Sena LA, and Chandel NS (2012). Physiological Roles of Mitochondrial Reactive Oxygen Species. Molecular Cell 48, 158–167. 10.1016/j.molcel.2012.09.025. [PubMed: 23102266]

94. Helmerhorst HJF, Arts DL, Schultz MJ, van der Voort PHJ, Abu-Hanna A, de Jonge E, and van Westerloo DJ (2017). Metrics of Arterial Hyperoxia and Associated Outcomes in Critical Care. Crit Care Med 45, 187–195. 10.1097/CCM.0000000000002084. [PubMed: 27763912]

95. Helmerhorst HJF, Roos-Blom M-J, van Westerloo DJ, and de Jonge E (2015). Association Between Arterial Hyperoxia and Outcome in Subsets of Critical Illness: A Systematic Review, Meta-Analysis, and Meta-Regression of Cohort Studies. Crit Care Med 43, 1508–1519. 10.1097/CCM.0000000000000998. [PubMed: 25855899]

96. Lui AY, Garber L, Vincent M, Celi L, Masip J, Sionis A, Serpa Neto A, Keller N, Morrow DA, Miller PE, et al. (2020). Hyperoxia is associated with adverse outcomes in the cardiac intensive care unit: insights from the Medical Information Mart for Intensive Care (MIMI-III) database. European Heart Journal 41, ehaa946.1837. 10.1093/ehjci/ehaa946.1837.

97. Palmer E, Post B, Klapaukh R, Marra G, MacCallum NS, Brealey D, Ercole A, Jones A, Ashworth S, Watkinson P, et al. (2019). The Association between Supraphysiologic Arterial Oxygen Levels and Mortality in Critically Ill Patients. A Multicenter Observational Cohort Study. Am J Respir Crit Care Med 200, 1373–1380. 10.1164/rccm.201904-0849OC. [PubMed: 31513754]

98. Cabello JB, Burls A, Emparanza JI, Bayliss SE, and Quinn T (2016). Oxygen therapy for acute myocardial infarction. Cochrane Database Syst Rev 12, CD007160. 10.1002/14651858.CD007160.pub4. [PubMed: 27991651]

99. Stoller JK, Panos RJ, Krachman S, Doherty DE, Make B, and Long-term Oxygen Treatment Trial Research Group (2010). Oxygen therapy for patients with COPD: current evidence and the long-term oxygen treatment trial. Chest 138, 179–187. 10.1378/chest.09-2555. [PubMed: 20605816]

100. Michiels C, Raes M, Toussaint O, and Remacle J (1994). Importance of Se-glutathione peroxidase, catalase, and Cu/Zn-SOD for cell survival against oxidative stress. Free Radic Biol Med 17, 235–248. 10.1016/0891-5849(94)90079-5. [PubMed: 7982629]

101. Ransy C, Vaz C, Lombès A, and Bouillaud F (2020). Use of H2O2 to Cause Oxidative Stress, the Catalase Issue. Int J Mol Sci 21. 10.3390/ijms21239149.

102. Bates DM, Popescu CV, Khoroshilova N, Vogt K, Beinert H, Münck E, and Kiley PJ (2000). Substitution of leucine 28 with histidine in the Escherichia coli transcription factor FNR results in increased stability of the [4Fe-4S](2+) cluster to oxygen. J Biol Chem 275, 6234–6240. 10.1074/jbc.275.9.6234. [PubMed: 10692418]

103. Ast T, Meisel JD, Patra S, Wang H, Grange RMH, Kim SH, Calvo SE, Orefice LL, Nagashima F, Ichinose F, et al. (2019). Hypoxia Rescues Frataxin Loss by Restoring Iron Sulfur Cluster Biogenesis. Cell 177, 1507–1521.e16. 10.1016/j.cell.2019.03.045. [PubMed: 31031004]

104. Taylor EM, Broughton BC, Botta E, Stefanini M, Sarasin A, Jaspers NG, Fawcett H, Harcourt SA, Arlett CF, and Lehmann AR (1997). Xeroderma pigmentosum and trichothiodystrophy are associated with different mutations in the XPD (ERCC2) repair/transcription gene. Proc Natl Acad Sci U S A 94, 8658–8663. 10.1073/pnas.94.16.8658. [PubMed: 9238033]

105. Hawer H, Mendelsohn BA, Mayer K, Kung A, Malhotra A, Tuupanen S, Schleit J, Brinkmann U, and Schaffrath R (2020). Diphthamide-deficiency syndrome: a novel human developmental disorder and ribosomopathy. Eur J Hum Genet 28, 1497–1508. 10.1038/s41431-020-0668-y. [PubMed: 32576952]

106. Lee P, Chandel NS, and Simon MC (2020). Cellular adaptation to hypoxia through hypoxia inducible factors and beyond. Nat. Rev. Mol. Cell Biol 10.1038/s41580-020-0227-y.

107. Gilbert LA, Horlbeck MA, Adamson B, Villalta JE, Chen Y, Whitehead EH, Guimaraes C, Panning B, Ploegh HL, Bassik MC, et al. (2014). Genome-Scale CRISPR-Mediated Control of Gene Repression and Activation. Cell 159, 647–661. 10.1016/j.cell.2014.09.029. [PubMed: 25307932]

108. Fang X, Neyrinck AP, Matthay MA, and Lee JW (2010). Allogeneic human mesenchymal stem cells restore epithelial protein permeability in cultured human alveolar type II cells by secretion of angiopoietin-1. J Biol Chem 285, 26211–26222. 10.1074/jbc.M110.119917. [PubMed: 20554518]

109. Sanjana NE, Shalem O, and Zhang F (2014). Improved vectors and genome-wide libraries for CRISPR screening. Nature Methods 11, 783–784. 10.1038/nmeth.3047. [PubMed: 25075903]

110. Doneanu C, Chen W, and Mazzeo J (2011). UPLC/MS Monitoring of Water-Soluble Vitamin Bs in Cell Culture Media in Minutes

111. Sinha M, and Lowell CA (2016). Isolation of Highly Pure Primary Mouse Alveolar Epithelial Type II Cells by Flow Cytometric Cell Sorting. Bio Protoc 6, e2013. 10.21769/BioProtoc.2013.

112. Li W, Köster J, Xu H, Chen CH, Xiao T, Liu JS, Brown M, and Liu XS (2015). Quality control, modeling, and visualization of CRISPR screens with MAGeCK-VISPR. Genome Biology 16, 1–13. 10.1186/s13059-015-0843-6. [PubMed: 25583448]

113. Liberzon A, Subramanian A, Pinchback R, Thorvaldsdóttir H, Tamayo P, and Mesirov JP (2011). Molecular signatures database (MSigDB) 3.0. Bioinformatics 27, 1739–1740. 10.1093/bioinformatics/btr260. [PubMed: 21546393]

114. Pang Z, Chong J, Zhou G, de Lima Morais DA, Chang L, Barrette M, Gauthier C, Jacques P-É, Li S, and Xia J (2021). MetaboAnalyst 5.0: narrowing the gap between raw spectra and functional insights. Nucleic Acids Research, 1–9. 10.1093/nar/gkab382. [PubMed: 33275144]

HIGHLIGHTS:

- Mechanisms of oxygen toxicity identified using genome-wide CRISPR/Cas9 screen
- Hyperoxia leads to degradation of specific iron-sulfur cluster-containing proteins
- Identical iron-sulfur cluster-containing proteins are depleted in hyperoxic lung cells
- ETC degradation under hyperoxia decreases oxygen consumption, exacerbating hyperoxia

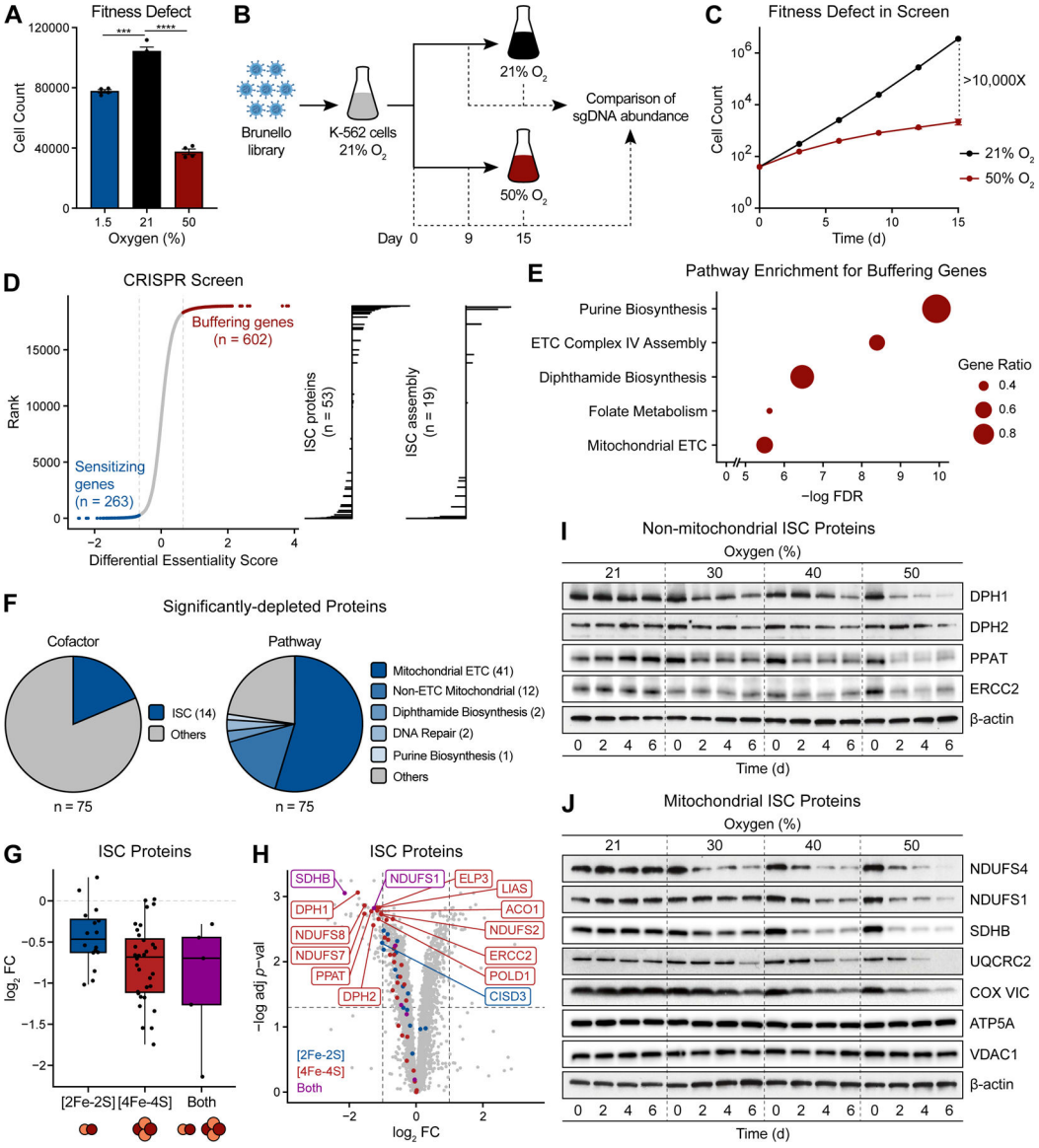

Figure 1. Genome-wide screen and proteomics identify pathways dependent on specific iron-sulfur cluster enzymes that are susceptible to oxygen toxicity.

A) K562 cell counts after 4 days at 1.5%, 21%, and 50% O_2 (***p<0.001, ****p<0.0001, unpaired t-test with Welch's correction, Mean +/− SEM). B) Genome-wide CRISPR screen design using Brunello library and exposure to 21% vs 80% O_2 (n=2 replicates). C) Cumulative growth of cells exposed to 21% versus 50% O_2 throughout the screen, (n=2). D) Gene ranking by essentiality in 21% versus 50% O_2 (MAGeCK-MLE algorithm). Bar plots (*right*) showing ISC-containing proteins and ISC assembly proteins relative to screen rankings. E) Enrichment analysis of buffering genes. F) Pie graph (*left*) and manually curated categories (*right*) of depleted proteins in hyperoxia. G) Box plot of different ISC levels in 50% O_2 relative to 21% O_2. H) Volcano plot highlighting depleted ISC-containing proteins in hyperoxia with a FC<0.5 ([2Fe-2S] proteins (blue), [4Fe-4S] proteins (red), both (purple) (Benjamini-Hochberg adjusted p-values). I) Validation of cytosolic/nuclear ISC

proteins sensitive to oxygen (21%-50% O_2) in K562 cells. J) Validation of oxygen-sensitive ETC proteins (21%-50% O_2) in K562 cells as a function of time and O_2.

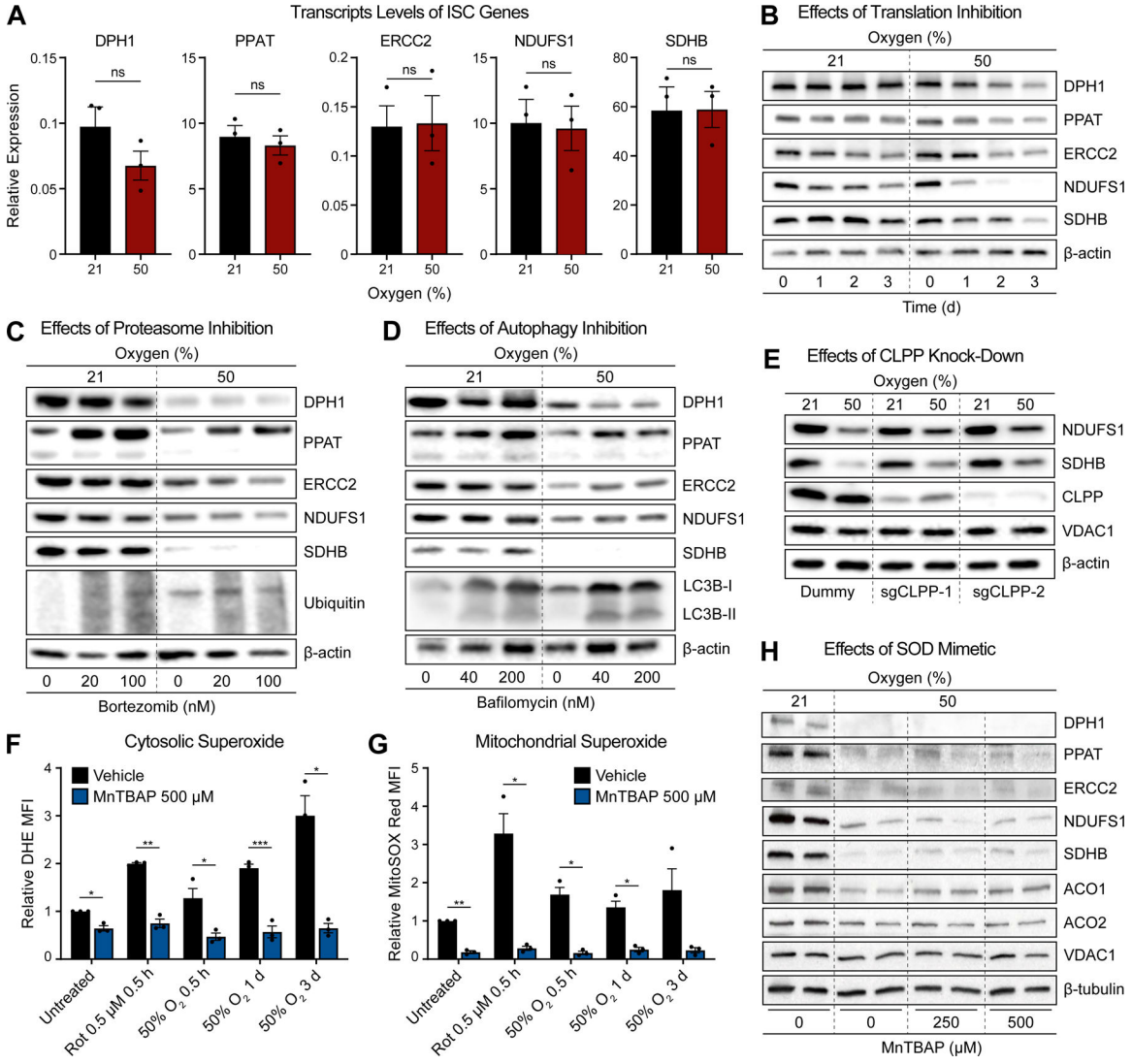

Figure 2. Protein degradation leads to depletion of specific ISC-containing proteins in hyperoxia that is not rescued by normalization of superoxide levels.

A) qPCR of relevant ISC genes in 21% versus 50% O_2 (n=3 biological replicates, unpaired t-test with Welch's correction). B) Levels of ISC proteins following exposure to 21% versus 50% O_2 and cycloheximide treatment for 0–3 days. C and D). Levels of ISC proteins following exposure to 21% versus 50% O_2 and to bortezomib or bafilomycin for last 12 hours of oxygen exposure. E) Effects of inducible CLPP knock down on select ETC protein levels (CI: NDUFS1, NDUFS2; CII: SDHB). F and G). DHE and MitoSOX measurements of K562 cells treated with the C I inhibitor rotenone or 50% O_2 for different timepoints. Cells were co-treated with vehicle or MnTBAP (unpaired t-test with Welch's correction). H). Levels of ISC proteins (following exposure to 21% versus 50% O_2 and MnTBAP for 3 days. All experiments performed in biological triplicate. Bar plots show mean +/− SEM. *p<0.05, **p<0.01, "ns" not significant.

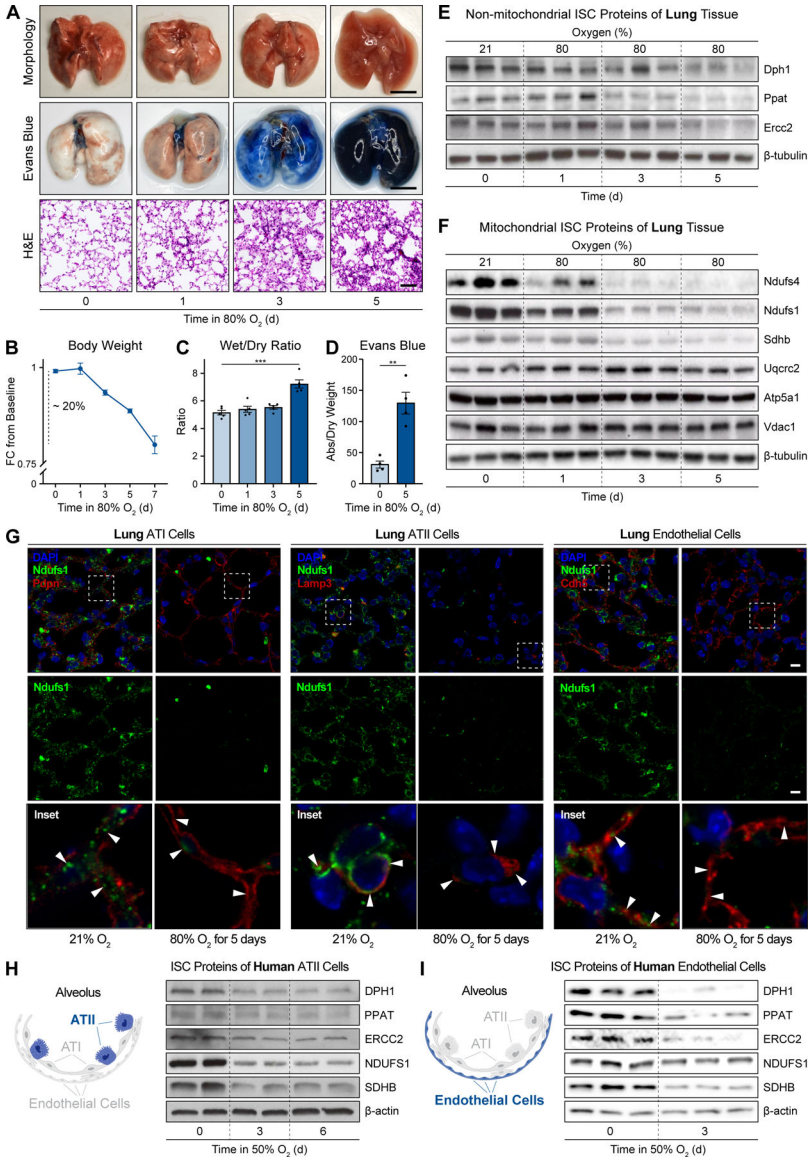

Figure 3. Hyperoxia induces acute lung injury in a mouse model and leads to degradation of specific ISC-containing proteins in mouse and human lung cells.

A) Whole lung images (*top;* scale bar: 500 μm), Evans blue extravasation (*middle;* scale bar: 500 μm), and H&E (15X) of lung (*bottom;* scale bar: 100 μm) from WT mice exposed to normoxia and 80% O_2,1–5 days. B) Mice body weights over time in 80% O_2. C) Wet-to-dry ratio and D) Evans blue dye quantification in same samples (n=5 per group, unpaired t-test with Welch's correction). E and F) Levels of ISC-containing non-ETC and ETC proteins from lung tissue from WT mice exposed to normoxia and 80% oxygen, 1–5 days (n=3 per group). G) Immunofluorescence (20X) from WT mice exposed to normoxia or 80% O_2 for 5 days, co-staining for the ISC-containing C I protein NDUFS1 (green) and lung cell markers (red): podoplanin (alveolar type I), lamp3 (alveolar type II), and cdh5/VE-cadherin (endothelial). DAPI (blue). White arrows (*bottom row*) point to NDUFS1 (Scale bar: 10 μm). Representative images shown. H, I) Non-ETC and ETC ISC-containing proteins from

primary human alveolar type II cells and endothelial cells exposed to normoxia and 50% O_2 for up to 6 days. Data shown as mean +/− SEM. **p<0.01, ***p<0.001.

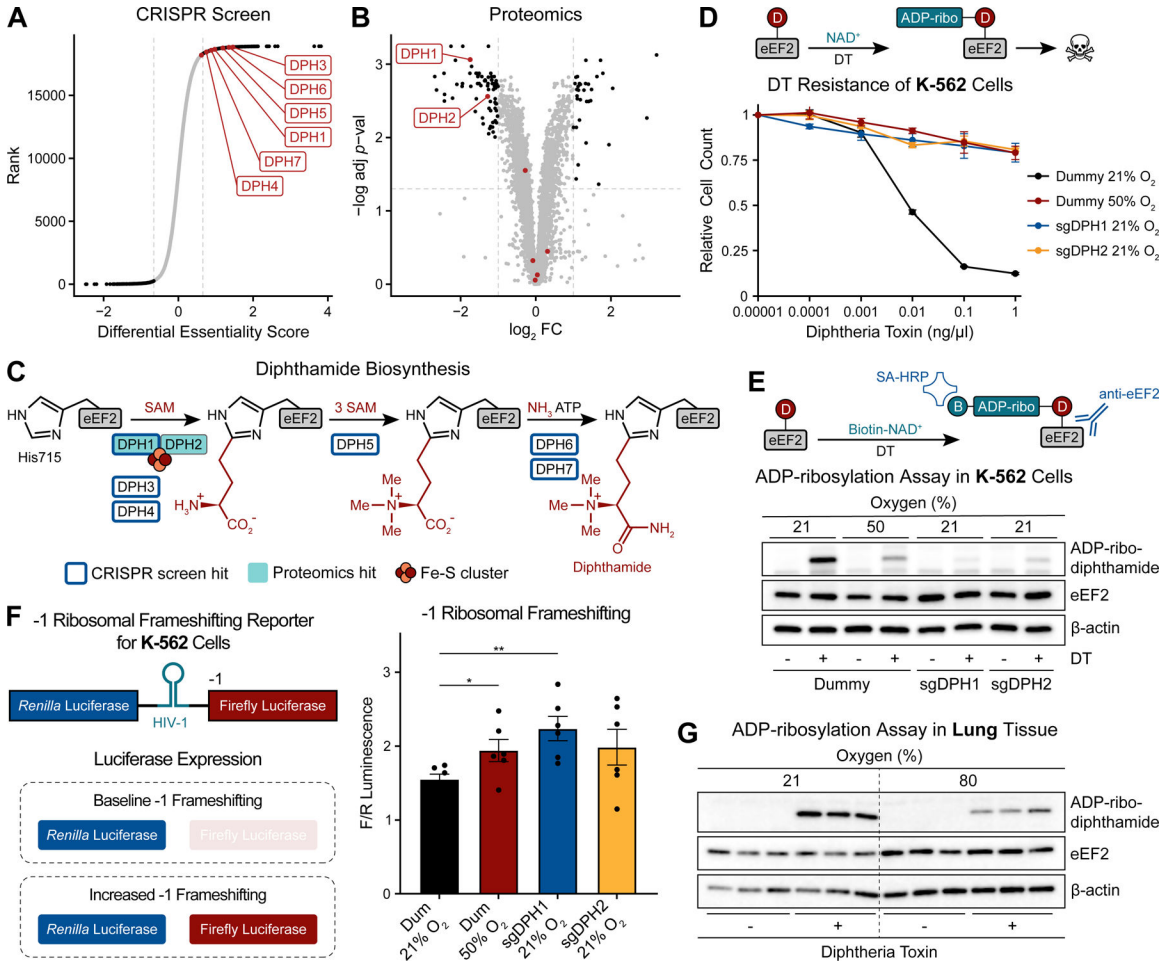

Figure 4. Hyperoxia decreases DPH1/DPH2 proteins, inhibits diphthamide biosynthesis, and increases ribosomal frameshifting.

A) DPH synthesis gene KOs are buffering hits. B) DPH synthesis enzymes are depleted in hyperoxia (Benjamini-Hochberg adjusted p-values). C) Role of the DPH proteins in diphthamide biosynthesis on the eukaryotic elongation factor (eEF2). CRISPR screen hits (blue outline), proteomics hits (turquoise box) and ISC are highlighted. D) Diphtheria-toxin (DT) resistance based on relative cell counts in K562 cells following KO of DPH1/DPH2 compared to normoxia and 50% O_2. E) Diphthamide synthesis based on ADP-ribosylation assay (see schematic) in K562 cells under normoxia or hyperoxia. F) Rates of −1 ribosomal frameshifting in K562 cells (*p<0.05, **p<0.01 by unpaired t-test with Welch's correction. Mean +/− SEM). G) ADP-ribosylation assay in lung tissue from WT mice exposed to normoxia versus 80% O_2 for 5 days (n=3). Experiments performed in at least biological triplicate.

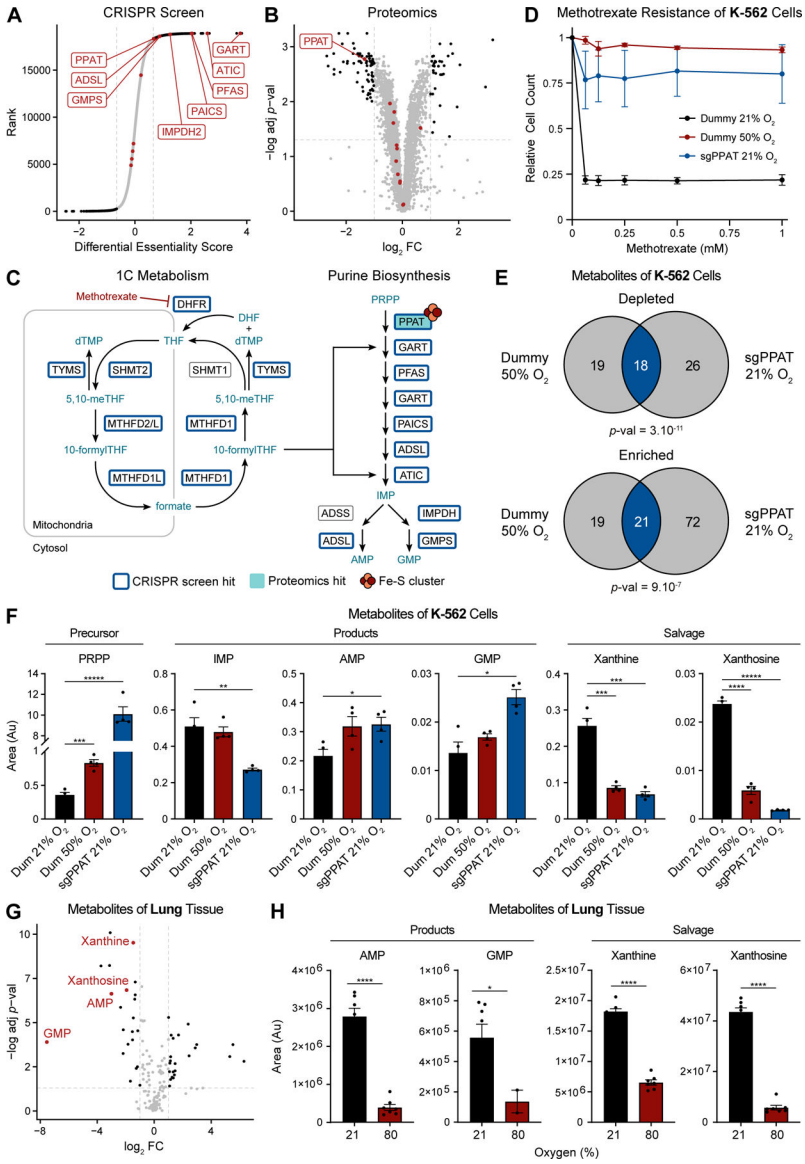

Figure 5. One carbon metabolism and purine synthesis are impaired in hyperoxia due to loss of SC-containing PPAT.

A) 1C metabolism and IMP biosynthesis gene KOs are buffering hits. B) ISC-containing PPAT is depleted in hyperoxia (Benjamini-Hochberg adjusted p-values). C) Schematic of 1C/purine biosynthesis pathways, showing CRISPR screen hits (blue outline), proteomics hits (turquoise box), and ISC. D) Hyperoxia and PPAT KO in normoxia confer resistance to methotrexate. E) Overlap of changing metabolites between hyperoxia-treated and PPAT KO cells. F) Purine synthesis and salvage pathway metabolite levels in 21% O_2, 50% O_2, and PPAT KO (n=4, unpaired t-test with Welch's correction). G) Volcano plot showing depleted metabolites in lung tissue from mice exposed to 80% O_2 for 5 days relative to normoxia. H) Metabolites in purine synthesis and salvage pathways in lung tissue from mice exposed to normoxia or 80% O_2, 5 days (n=7 mice each condition). Bar plots show mean +/− SEM. *p<0.05, **p<0.01, ***p<0.001, ****p<0.0001.

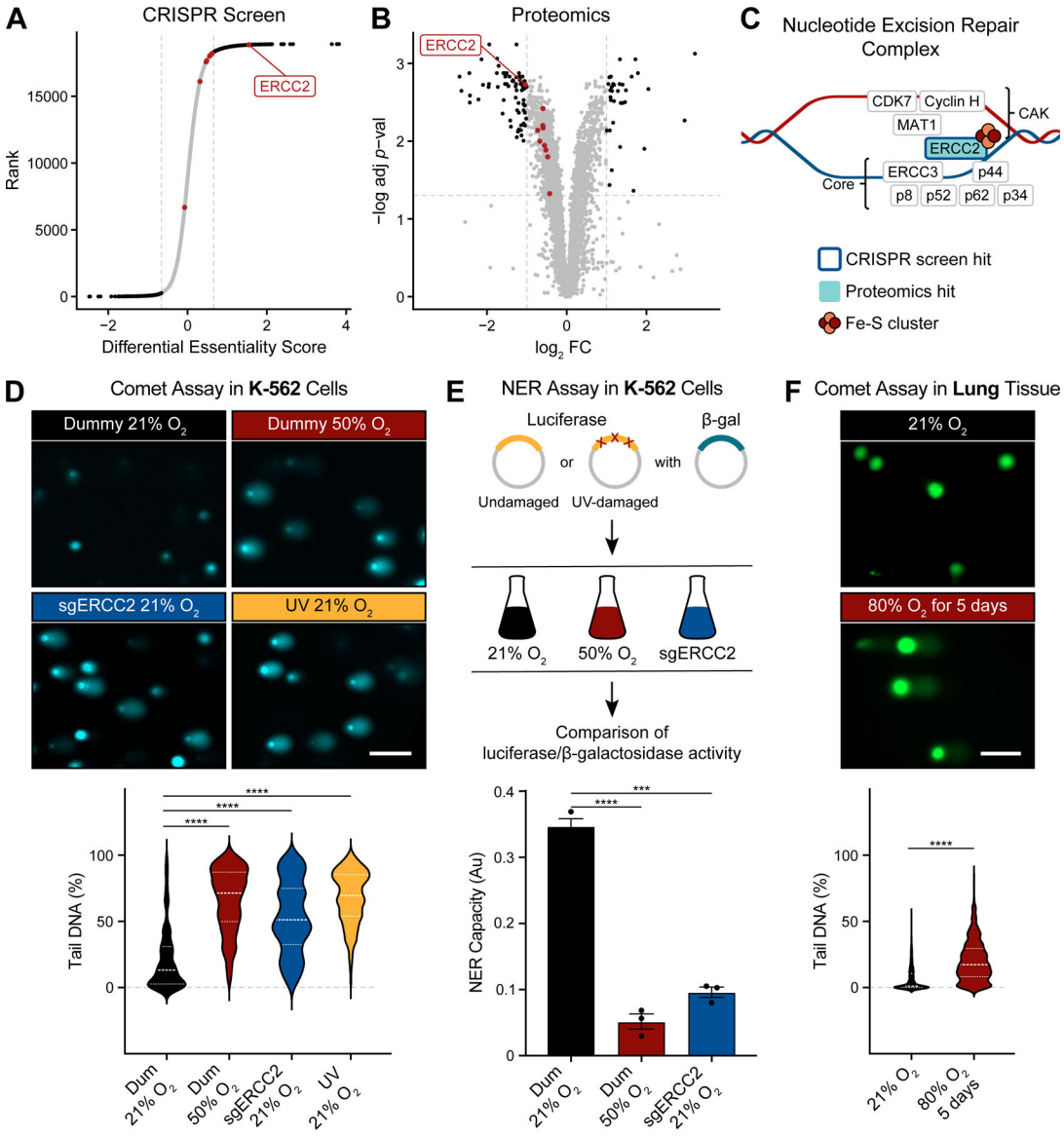

Figure 6. Nucleotide excision repair (NER) is compromised in hyperoxia due to loss of *ERCC2*/XPD.

A) Gene KOs in the TFIIH complex involved in transcription-coupled NER are buffering hits. B) The ISC-containing protein XPD (encoded by *ERCC2*) is depleted in hyperoxia (Benjamini-Hochberg adjusted p-values). C) Schematic of TFIIH multi-protein complex. CRISPR screen hits (blue outline), proteomics hits (turquoise box) and ISCs. D) Representative comet images of cells exposed to 21% versus 50% O_2, *ERCC2* KO or UV light. DNA damage quantified based on comet tail (% tail DNA) (unpaired t-test with Welch's correction). Scale bar: 500 μm. E) *In vitro* luciferase assay of NER in 50% O_2, 21% O_2, and *ERCC2* KO. n=3 replicates (unpaired t-test with Welch's correction. Mean +/− SEM). F) Representative comet images of single cells isolated from lung tissue from WT mice exposed to 21% versus 80% O_2, 5 days. DNA damage quantified based on DNA content in comet tail. Scale bar: 400 μm. ***p<0.001, ****p<0.0001.

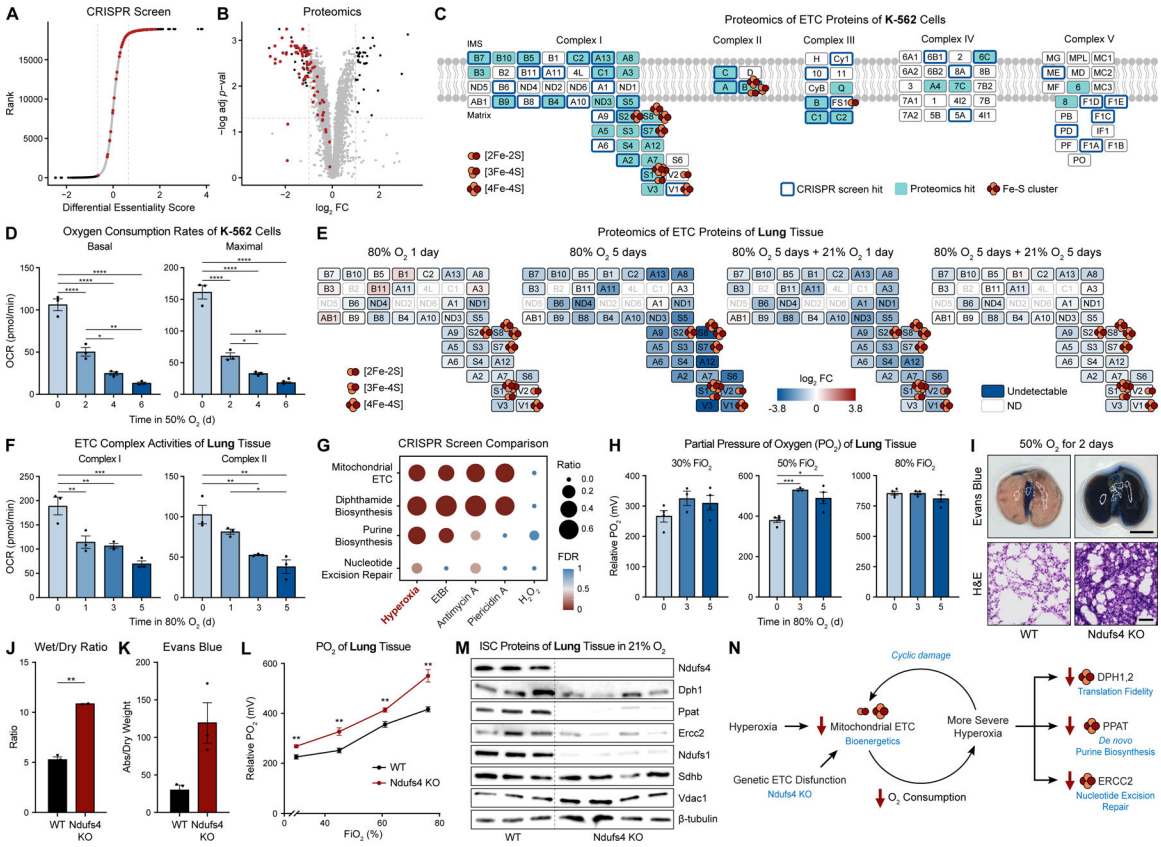

Figure 7. Hyperoxia decreases ETC proteins, leading to impaired ETC function and lung hyperoxia. Genetic ETC dysfunction causally demonstrates cyclic oxygen toxicity model.

A) S-plot of ETC genes (red dots) relative to buffering and sensitizing hits (black dots). B) ETC proteins (red dots) are depleted in hyperoxia (Benjamini-Hochberg adjusted p-values). C) Schematic of ETC (CI-V) depicting CRISPR screen hits (blue outline), proteomics hits (turquoise box), and ISCs. D) Basal and maximal oxygen consumption rates in hyperoxia vs. normoxia, K562 cells (n=3 replicates). E) Proteomics data schematic of ETC complex I proteins from lung tissue of WT mice exposed to normoxia or 80% O_2 (1 and 5 days), and WT mice exposed to 80% O_2 for 5 days then returned to 21% O_2 (n=6 per group). F) Complex I/II activity from mitochondria isolated from WTC57Bl/6 mice exposed to normoxia vs 80% O_2 for 1–5 days (Tukey's multiple comparisons test). G) Enrichment analysis of the most affected gene pathways in hyperoxia vs. normoxia genome-wide CRISPR screen compared to previously published genetic screens using piericidin A, antimycin A (ETC inhibitors), ethidium bromide (mt DNA replication inhibitor), and H_2O_2[83,84] using hypergeometric test. Circle radius represents gene ratio of overlapping top buffering genes in gene sets. H) *In vivo* lung tissue PO_2 measurements using Clark electrode (mV) from ventilated mice with various fraction of inspired oxygen (FiO_2) following exposure to 21% versus 80% O_2 for 3 and 5 days (unpaired t-test with Welch's correction). I) Evans blue dye extravasation (*top*; scale bar: 500 μm) and H&E images (*bottom*; scale bar: 100 μm) of lung tissue from WT and *Ndufs4* KO mice exposed to 50% O_2, 2 days. J) Lung wet-to-dry ratio from WT and *Ndufs4* KO mice exposed to normoxia and 50% oxygen, 2d (n=3 per group). K) Evans blue dye quantification from same samples L) Lung

tissue PO_2 measurements (mV) from ventilated WT and *Ndufs4* KO mice (P35–40) with different fraction of inspired oxygen (FiO_2)(unpaired t-test with Welch's correction). M) ETC and non-ETC ISC-containing proteins from lung tissue in WT and *Ndufs4* KO mice (P40–45) at 21% O_2 (n=3 WT; n=4 *Ndufs4* KO). N) Model of cyclic oxygen toxicity. Bar plots show mean +/− SEM. *p<0.05, **p<0.01, ***p<0.001, ****p<0.0001.

KEY RESOURCES TABLE

REAGENT or RESOURCE	SOURCE	IDENTIFIER
Antibodies		
Antibodies for western blotting see Table S4	This paper	N/A
Bacterial and Virus Strains		
Brunello Human CRISPR Knockout Pooled Library	Doench et al., 2016	73179-LV
Chemicals, Peptides, and Recombinant Proteins		
Diphtheria Toxin	Millipore Sigma	D0564
6-Biotin-17-NAD	Trevigen	4670–500-01
Lipofectamine LTX	Thermo Fisher	15338100
Methotrexate hydrate	Sigma-Aldrich	A6770
Cycloheximide	NETA SCIENTIFIC Inc	RPI-C81040–1.0
Bortezomib	Sigma-Aldrich	5043140001
Bafilomycin A1	Sigma-Aldrich	19–148
Critical Commercial Assays		
Comet Assay Kit	Abcam	ab238544
Dual-Glo Luciferase Assay System	Promega	E2920
CellTiter-Glo Luminescent Cell Viability Assay	Promega	G7573
Deposited Data		
Genome-wide CRISPR KO screen under hyperoxia	This paper	SRA: PRJNA931848
ETC inhibition CRISPR KO screen	To et al., 2019	N/A
H_2O_2 CRISPR KO screen	Dubreuil et al., 2020	N/A
K562 proteomics	This paper	MSV000091206
Hyperoxia lung proteomics	This paper	MSV000091206
K562 metabolomics under hyperoxia or PPAT KO	This paper	MTBLS7039
Hyperoxia lung metabolomics	This paper	MTBLS7039
Unprocessed blots, gel, and images	This paper	DOI: 10.17632/ykcyz2sdx2.1
Experimental Models: Cell Lines		
K562 cells	ATCC	CCL-243
293T cells	ATCC	CRL-3216
Experimental Models: Organisms/Strains		
C57BL/6J	Jackson Laboratory	000664
Oligonucleotides		
Primer sequences for qPCR see Table S4	This paper	N/A
sgRNA sequences for generating KO cells see Table S4	This paper	N/A
Recombinant DNA		
lentiCRISPR v2	Sanjana, Shalem and Zhang, 2014	52961
HIV-1 minus one frameshift reporter	This paper	pAGH10 (Addgene #198224)

REAGENT or RESOURCE	SOURCE	IDENTIFIER
Ty1 plus one frameshift reporter	This paper	pAGH11 (Addgene #198225)
pGL3 Luciferase Reporter	Promega	E1751
pSV-β-Galactosidase	Promega	E1081
Software and Algorithms		
MAGeCK 0.5.8	Li et al., 2015	https://sourceforge.net/projects/mageck/
MAGeCKFlute 0.99.18	Wang et al., 2019	10.18129/B9.bioc.MAGeCKFlute
MaxQuant software v1.5.5.1	Max Planck Institute of Biochemistry	https://www.maxquant.org/
Compound Discoverer 3.1	Thermo Fisher	https://www.thermofisher.com/us/en/home/industrial/mass-spectrometry/liquid-chromatography-mass-spectrometry-lc-ms/lc-ms-software/multi-omics-data-analysis/compound-discoverer-software.html
MetaboAnalyst 5.0	Pang et al., 2021	https://www.metaboanalyst.ca
COMET Score 2.0	Rex Hoover	http://rexhoover.com/index.php?id=cometscore